

Gravity-driven Lyman-alpha blobs from cold streams into galaxies

Tobias Goerdt^{1*}, A. Dekel^{1†}, A. Sternberg^{2‡}, D. Ceverino^{1§}, R. Teyssier^{3¶} & J. R. Primack^{4||}

¹*Racah Institute of Physics, The Hebrew University, Jerusalem 91904, Israel*

²*The Raymond and Beverly Sackler School of Physics and Astronomy, Tel Aviv University, Tel Aviv 69978, Israel*

³*Institut für Theoretische Physik, Universität Zürich, Winterthurer Strasse 190, CH-8057 Zürich, Schweiz*

⁴*Department of Physics, University of California, Santa Cruz, CA 95064, USA*

Draft version 6 November 2018

ABSTRACT

We use high-resolution cosmological hydrodynamical AMR simulations to predict the characteristics of $L\alpha$ emission from the cold gas streams that fed galaxies in massive haloes at high redshift. The $L\alpha$ luminosity in our simulations is powered by the release of gravitational energy as gas flows from the intergalactic medium into the halo potential wells. The UV background contributes only $< 20\%$ to the gas heating. The $L\alpha$ emissivity is due primarily to electron-impact excitation cooling radiation in gas $\sim 2 \times 10^4$ K. We calculate the $L\alpha$ emissivities assuming collisional ionisation equilibrium (CIE) at all gas temperatures. The simulated streams are self-shielded against the UV background, so photoionisation and recombination contribute negligibly to the $L\alpha$ line formation. We produce theoretical maps of the $L\alpha$ surface brightnesses, assuming that $\sim 85\%$ of the $L\alpha$ photons are directly observable. We do not consider transfer of the $L\alpha$ radiation, nor do we include the possible effects of internal sources of photoionisation such as star-forming regions. Dust absorption is expected to obscure a small fraction of the luminosity in the streams. We find that typical haloes of mass $M_v \sim 10^{12-13} M_\odot$ at $z \sim 3$ emit as $L\alpha$ blobs (LABs) with luminosities $10^{43-44} \text{ erg s}^{-1}$. Most of the $L\alpha$ comes from the extended (50–100 kpc) narrow, partly clumpy, inflowing, cold streams of $(1-5) \times 10^4 \text{ K}$ that feed the growing galaxies. The predicted LAB morphology is therefore irregular, with dense clumps and elongated extensions. The integrated area contained within surface-brightness isophotes of $2 \times 10^{-18} \text{ erg s}^{-1} \text{ cm}^{-2} \text{ arcsec}^{-2}$ is $\sim 2-100 \text{ arcsec}^2$, consistent with observations. The linewidth is expected to range from 10^2 to more than 10^3 km s^{-1} with a large variance. The typical $L\alpha$ surface brightness profile is $\propto r^{-1.2}$ where r is the distance from the halo centre. Our simulated LABs are similar in luminosity, morphology and extent to the observed LABs, with distinct kinematic features. The predicted $L\alpha$ luminosity function is consistent with observations, and the predicted areas and linewidths roughly recover the observed scaling relations. This mechanism for producing LABs appears inevitable in many high- z galaxies, though it may work in parallel with other mechanisms. Some of the LABs may thus be regarded as direct detections of the cold streams that drove galaxy evolution at high z .

Key words: cosmology — galaxies: evolution — galaxies: formation — galaxies: high redshift — intergalactic medium — galaxies: ISM

1 INTRODUCTION

Hundreds of Lyman-alpha blobs (LAB) have been detected so far in the redshift range $z = 2-6.5$, mostly near $z \sim 3$ (Steidel et al. 2000; Matsuda et al. 2004; Saito et al. 2006; Ouchi et al. 2009; Yang et al. 2008). Their luminosities

* tgoerdt@phys.huji.ac.il
 † dekel@phys.huji.ac.il
 ‡ amiel@wise.tau.ac.il
 § ceverino@phys.huji.ac.il
 ¶ teyssier@physik.uzh.ch
 || joel@scipp.ucsc.edu

range from below 10^{43} to above 10^{44} ergs $^{-1}$, and they extend on the sky to 30 – 50 kpc and more. The two main open questions are (a) the origin of the extended cold and relatively dense gas capable of emitting $L\alpha$, and (b) the continuous energy source for exciting the gas to emit $L\alpha$.

The emitting hydrogen gas should be at a temperature $T \gtrsim 10^4$ K, relatively dense and span a much larger area than covered by the stellar component of galaxies. It may arise from outflows or inflows. The energy sources discussed in the literature include photoionisation by obscured AGNs, early starbursts or extended X-ray emission (Haiman & Rees 2001; Jimenez & Haiman 2006; Scharf et al. 2003), as well as compression of ambient gas by superwinds to dense $L\alpha$ emitting shells (Mori et al. 2004), and star formation triggered by relativistic jets from AGNs (Rees 1989).

Many of the bright LABs are found in the vicinity of massive, star-forming galaxies (Matsuda et al. 2006). Multi-wavelength observations reveal that a fraction of the LABs are associated with sub-millimetre and infrared sources that indicate very high star-formation rates (SFR) in the range $10^2 - 10^3 M_{\odot} \text{yr}^{-1}$ (Chapman et al. 2001; Geach et al. 2005, 2007) or with obscured active galactic nuclei (AGN) (Basu-Zych & Scharf 2004; Scarlata et al. 2009). While stellar feedback and AGNs could in principle provide the energy source for the $L\alpha$ luminosity, many LABs are not associated with sources of this sort that are powerful enough to explain the observed $L\alpha$ luminosities (Nilson et al. 2006; Smith & Jarvis 1999). This indicates that star formation and AGNs are not the sole drivers of LABs, and may not even be the dominant source for LABs.

Indeed, high-redshift galaxies exhibit a generic mechanism that simultaneously provides both the cold gas and the energy source. It is a direct result of the phenomenon robustly established by simulations and theoretical analysis, where high- z massive galaxies are continuously fed by narrow, cold, intense, partly clumpy, gaseous streams that penetrate through the shock-heated halo gas into the inner galaxy, grow a dense, unstable, turbulent disc with a bulge and trigger rapid star formation (Birnboim & Dekel 2003; Keres et al. 2005; Dekel & Birnboim 2006; Ocvirk, Pichon & Teyssier 2008; Keres et al. 2009; Dekel et al. 2009; Johansson, Naab & Ostriker 2009; Dekel, Sari & Ceverino 2009; Ceverino, Dekel & Bournaud 2009). Massive clumpy star-forming disks observed at $z \sim 2$ (Genzel et al. 2008; Genel et al. 2008; Förster Schreiber et al. 2009) may have been formed via the smooth and steady accretion provided by cold flows, as opposed to merger events. The streaming of the gas into the dark-matter halo potential well is associated with transfer of gravitational energy to excitations of the hydrogen atoms followed by cooling emission of $L\alpha$ (Haiman, Spaans & Quataert 2000; Fardal et al. 2001; Dekel & Birnboim 2006, 2008; Khochfar & Ostriker 2008; Furlanetto et al. 2003, 2005).

There were two earlier attempts to compute the $L\alpha$ cooling radiation from hydrodynamic SPH cosmological simulations. Based on their analysis, Fardal et al. (2001) pointed out the potential association of this $L\alpha$ cooling emission with the first observed LABs. These early simulations did not allow a proper resolution of the detailed structure of the cold streams as they penetrate through the hot medium. Their shortcomings included intrinsic

limitations of the SPH technique, a limited force resolution of $7 h^{-1}$ kpc (comoving), not allowing for radiative cooling below 10^4 K and neglecting the photoionisation by the UV background. Furlanetto et al. (2005) used SPH simulations with a somewhat higher resolution of ~ 1 kpc to make more detailed comparisons of the simulated and observed luminosity functions and size distributions of LABs powered by cold accretion. In their pessimistic model, assuming no emissivity from gas that is self-shielded from the ionising background radiation, they end up with low $L\alpha$ luminosity. They comment that cooling IGM gas may explain the observations only if one adopts an optimistic scenario, where the self-shielded gas is emitting $L\alpha$ at CIE. The latter scenario will also be adopted in this paper. Other sources of ionisation are ignored and radiative transfer is not applied.

Dijkstra & Loeb (2009, hereafter DL09) have recently worked out an analytic toy model for $L\alpha$ cooling radiation from cold streams, based on the general properties of the cold streams as reported from cosmological simulations. They conclude that the streams could in principle provide spatially extended $L\alpha$ sources with luminosities, line widths and abundances that are similar to those of observed LABs. They point out that the filamentary structure of cold flows may explain the wide range of observed LAB morphologies. They also highlight the fact that the most luminous cold flows are associated with massive haloes, which preferentially reside in dense large-scale surroundings, in agreement with the observed presence of bright LABs in dense environments. This model presents a successful feasibility test for the role of cold streams in powering the LAB emission, and it provides physical intuition into the way by which this process could be manifested. However, a comparison to our simulations indicates that this simplified model does not capture the detailed hydrodynamic properties of the cold streams. In particular, it significantly over-predicts the cold-gas density, under-predicts the gas temperature, and does not account for the partly clumpy nature of the streams and their characteristic radial distribution in the halo. As a result, the DL09 model underestimates the total $L\alpha$ luminosity by a factor of a few, and it therefore has to appeal to the excessive clustering of the LABs in order to boost up the predicted luminosity function for a match with the observations.

In the current paper, we calculate the $L\alpha$ emission from the cold gas in high-redshift galactic haloes using state-of-the-art hydrodynamical AMR cosmological simulations. With a maximum resolution better than 70 pc in our simulations we can quite accurately map the extended $L\alpha$ sources. This allows us to study their individual shapes, morphologies and kinematics. We measure quantities such as the distribution of surface brightness within each halo, the area covered with surface brightness above a given isophotal threshold, the predicted observed linewidth, the typical total $L\alpha$ luminosity per halo of a given mass, and the overall $L\alpha$ luminosity function of LABs. These predicted properties are compared with the observed LABs.

This paper is organised as follows. In §2 we work out a simple feasibility test where we use a simple toy model to estimate the expected gravitational heating power as a proxy for the $L\alpha$ luminosity. In §3 we introduce the two sets of cosmological simulations used. In §4 we explain our methodology of computing $L\alpha$ emissivity

and luminosity as a function of halo mass. In §5 we identify the gas that contributes to the $L\alpha$ emission. In §6 we apply our methodology to the simulations and provide predicted images of LABs. In §7 we determine the scaling of $L\alpha$ luminosity as a function of halo mass and redshift. In §8 we compare our predicted $L\alpha$ luminosity function with observational results. In §9 we measure the predicted surface-density profile, isophotal area and linewidth and compare to observations. In §10 we show that gravitational heating is the main source of energy driving the $L\alpha$ luminosity in our simulations, while the role of photoionisation is minor. In §11 we discuss our analysis and results and draw our conclusions.

2 FEASIBILITY OF GRAVITATIONAL HEATING

The gravitational energy gain due to the streaming of the gas from the virial radius toward the centre of the halo potential well is a natural source of energy for the $L\alpha$ emission. The gravitational energy released per unit infalling mass is of order $V_v^2 = GM_v/R_v$, where the quantities are the virial velocity, mass and radius respectively. The accretion rate \dot{M} can be estimated from the observed star-formation rate. For $V \sim 300 \text{ km s}^{-1}$ and $\dot{M} \sim 150 M_\odot \text{ yr}^{-1}$ we obtain a power $\dot{M} V^2 \sim 10^{43} \text{ erg s}^{-1}$, comparable to the luminosity of a typical LAB.

In some more detail, an analysis of the MN cosmological simulation (described below in §3) reveals that both the cold gas accretion rate \dot{M}_c and its inward velocity are roughly constant along the streams (Dekel et al. 2009). If so, the gravitational power deposited at radius r per unit radial length in the cold gas is

$$\dot{E}_{\text{grav}} = f_c \dot{M}_c \left| \frac{\partial \phi}{\partial r} \right|, \quad (1)$$

where $\phi(r)$ is the gravitational potential at r . The factor f_c is the fraction of the energy that goes to heating the cold streams themselves rather than the hot medium. The total power deposited between the virial radius R_v and radius r , across a potential difference $\Delta\phi(R_v, r)$, is

$$\dot{E}_{\text{grav}} = f_c \dot{M}_c |\Delta\phi(R_v, r)|. \quad (2)$$

Given the total mass density profile $\rho(r)$ and the associated mass profile $M(r)$, the potential gain is

$$|\Delta\phi| \equiv \hat{\phi} V_v^2, \quad \hat{\phi} = -1 + \frac{V^2(r)}{V_v^2} + \int_{r/R_v}^1 \frac{3\rho(r')}{\bar{\rho}_v} r' dr', \quad (3)$$

where $V^2(r) = GM(r)/r$, $\bar{\rho}_v$ is the mean density within the virial radius, and $\hat{\phi}$ is typically a number of order unity.

For an NFW potential well with a concentration parameter C (Navarro, Frenk & White 1997), one has

$$\hat{\phi}(r) = \frac{C}{A_1(C)} \left[\frac{\ln(1+x)}{x} - \frac{\ln(1+C)}{C} \right], \quad (4)$$

where $x = Cr/R_v$ and $A_1(x) = \ln(x+1) - x/(x+1)$. According to cosmological N -body simulations (Bullock et al. 2001), the average concentration parameter as a function of halo mass and redshift is $C \simeq 3 M_{12}^{-0.13} (1+z)_4^{-1}$, where $M_{12} \equiv M_v/10^{12} M_\odot$ and $(1+z)_4 \equiv (1+z)/4$.

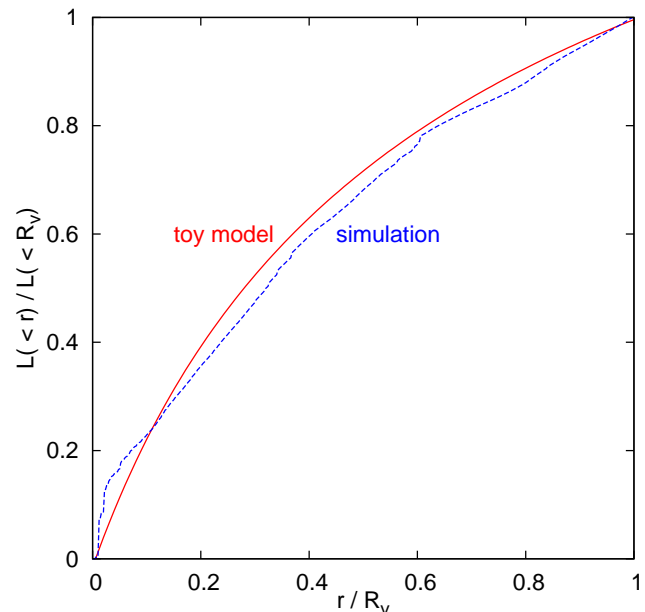


Figure 1. Cumulative luminosity profile, showing the fraction of the luminosity from within a sphere of radius r compared to the virial sphere. The toy-model prediction (solid red) is proportional to the fraction of gravitational energy that is deposited inside radius r based on eq. (8). The predicted profile in the range $(0.2 - 0.5)R_v$ can be approximated by the power law $L(<r) \propto r^{0.7}$. About half the luminosity is expected to originate from the cold streams in the halo outside the inner $0.27R_v$ sphere. Shown in comparison is the luminosity profile as derived from the three simulated CDB galaxies stacked together (see section 10). The similarity between the toy model predictions and the simulation results is remarkable.

For $M_v = 10^{12} M_\odot$, this is $C \simeq 3$ at $z = 3$. Then $\hat{\phi}(r) \simeq 4.7 [\ln(1+x)/x - 0.46]$ so $\hat{\phi}(x \rightarrow 0) \simeq 2.5$.

A practical approximation for the average accretion rate into haloes of $M_v \sim 10^{12-13} M_\odot$ in the standard Λ CDM cosmology¹ is derived from the EPS approximation and from the Millennium cosmological simulation (Neistein, van den Bosch & Dekel 2006; Neistein & Dekel 2008; Birnboim, Dekel & Neistein 2007, Appendix A). The same MN hydrodynamical simulation that is used in the current paper (§3) reveals that 95% of the gas accretion is through cold streams that penetrate efficiently all the way into the vicinity of the central galaxy. For a baryonic fraction of 0.165 in the incoming streams, the average cold accretion rate is approximated by

$$\dot{M}_c \simeq 137 M_\odot \text{ yr}^{-1} M_{12}^{1.15} (1+z)_4^{2.25}. \quad (5)$$

This accretion rate is consistent with the typical SFR of $\sim 100 M_\odot \text{ yr}^{-1}$ observed in massive galaxies of similar comoving number densities at redshifts 2 – 3 (Genzel et al. 2006; Förster Schreiber et al. 2006; Elmegreen et al. 2007; Genzel et al. 2008; Stark et al. 2008).

The virial velocity is given by²

¹ Adopting the parameters motivated by WMAP5: $\Omega_m = 0.28$, $\Omega_\Lambda = 0.72$, $h = 0.7$, $\sigma_8 = 0.8$.

² With $R_v \simeq 77 \text{ kpc} M_{12}^{1/3} (1+z)_4^{-1}$, for completeness.

$$V_v \simeq 236 \text{ km s}^{-1} M_{12}^{1/3} (1+z)_4^{1/2}, \quad (6)$$

so we finally obtain in eq. (2)

$$\dot{E}_{\text{grav}} \simeq 1.2 \times 10^{43} \text{ erg s}^{-1} f_c M_{12}^{1.82} (1+z)_4^{3.25}. \quad (7)$$

Assuming that a substantial fraction f_α of this energy is emitted as observable $L\alpha$ radiation, we conclude that at $z \sim 3$, with $f_\alpha f_c \sim 1$, a LAB of luminosity $L \sim 10^{43} \text{ erg s}^{-1}$ is feasible from haloes of $M_v \sim 10^{12} M_\odot$. Luminosities as high as $\sim 10^{44} \text{ erg s}^{-1}$ require haloes of $\sim 3 \times 10^{12} M_\odot$. If $f_\alpha f_c$ is only ~ 0.1 , then the required haloes for the same luminosities are about three times more massive. We note that the mean comoving number density for haloes more massive than $(1, 3, 10) \times 10^{12} M_\odot$ at $z = 3$ is $(4.7, 0.68, 0.057) \times 10^{-4} \text{ Mpc}^{-3}$ respectively. Given that LABs of a luminosity higher than $10^{43} \text{ erg s}^{-1}$ appear with a comoving number density of $\sim 5 \times 10^{-5} \text{ Mpc}^{-3}$ (Fig. 14), the simple gravitational heating model indicates that they can emerge from haloes of $\sim 3 \times 10^{12} M_\odot$, with $f_\alpha f_c \sim 0.1$. Thus, the comparison of the estimates from our toy model with the total luminosities of the observed LABs indicates that gravitational heating is a feasible source for the $L\alpha$ emission. This kind of energy has to be released from these galaxies.

One can combine equations (4) and (7) to evaluate the gravitational energy deposited at different radii,

$$\begin{aligned} \dot{E}_{\text{grav}}(< r) &\simeq 1.2 \times 10^{43} \text{ erg s}^{-1} f_c M_{12}^{1.82} (1+z)_4^{3.25} \\ &\times \left[1.86 - \frac{1.86 \ln(1 + Cr/R_v)}{Cr/R_v} \right]. \end{aligned} \quad (8)$$

This gives a very crude estimate for the 3D luminosity profile $L(< r) = f_\alpha f_c \dot{E}_{\text{grav}}(< r)$. This profile is shown in Fig. 1, normalised to the total luminosity inside the virial radius. One can read from this plot the fraction of the luminosity that is expected in the different zones of the halo. For example, about half the luminosity is expected from outside $r = 0.27 R_v$, implying that in haloes of $M_v \sim 10^{12} M_\odot$ the LABs are expected to extend over more than 50 kpc. The luminosity profile predicted by gravitational heating is to be compared with our results from the simulations (§10), and with observed LABs (§9).

3 SIMULATIONS

We use here simulated galaxies from two different suites of simulations, both employing Eulerian Adaptive Refinement Tree (AMR) hydrodynamics in a cosmological setting. One suite consists of three simulations zooming in with a maximum resolution of 35 – 70 pc on individual galaxies that reside in dark-matter haloes of masses $\sim 5 \times 10^{11} M_\odot$ at $z = 2.3$ (Ceverino, Dekel & Bournaud 2009, hereafter CDB). The other suite is from the Horizon MareNostrum simulation containing hundreds of massive galaxies in a cosmological box of side $50 h^{-1} \text{ Mpc}$ with a maximum resolution of $\simeq 1 \text{ kpc}$ (Ocvirk, Pichon & Teyssier 2008, hereafter MN).

Figure 2 shows sample gas density maps of galaxies from the two suites of simulations. They demonstrate the dominance of typically three, narrow cold streams, which come from well outside the virial radius along the dark-matter filaments of the cosmic web, and penetrate

into the discs at the halo centres. The streams are partly clumpy and partly smooth, even in the simulation of higher resolution. The typical densities in the streams are in the range $n = 0.01 - 0.1 \text{ cm}^{-3}$, and they reach $n = 0.1 - 1 \text{ cm}^{-3}$ at the clump centres and in the central disk.

3.1 High-resolution ART CDB simulations

The CDB simulations have been run with the AMR tree code ART (Kravtsov, Klypin & Khokhlov 1997; Kravtsov 2003) with a spatial resolution better than 70 pc in physical units. The code incorporates the relevant physical processes for galaxy formation, including gas cooling and photoionisation heating, star formation, metal enrichment and stellar feedback (Ceverino & Klypin 2009). Cooling rates were computed for the given gas density, temperature, metallicity, and UV background based on CLOUDY (Ferland et al. 1998), assuming cooling at the centre of a cloud of thickness 1 kpc (Ceverino-Rodriguez 2008; Robertson & Kravtsov 2008). Metals are included, assuming an abundance of 0.02 relative to the total mass for a solar composition. The code implements a “constant” feedback model, in which the combined energy from stellar winds and supernova explosions is released as a constant heating rate over 40 Myr, the typical age of the lightest star that explodes as a type-II supernova. Photo-heating is also taken into account self-consistently with radiative cooling. A uniform UV background based on the Haardt & Madau (1996) model is assumed, local sources are ignored. In order to mimic the self-shielding of dense, galactic neutral hydrogen from the cosmological UV background, the simulation assumes a substantially suppressed UV background ($5.9 \times 10^{26} \text{ erg s}^{-1} \text{ cm}^{-2} \text{ Hz}^{-1}$, the value of the pre-reionisation UV background at $z = 8$) for the gas at total gas densities above $n = 0.1 \text{ cm}^{-3}$.

The unique feature of this code for the purpose of simulating the detailed structure of the streams and the gravitational instability in the disk is to allow the gas to cool down well below 10^4 K , thus reaching high densities in pressure equilibrium with the hotter and more dilute medium. A non-thermal pressure floor has been implemented to ensure that the the Jeans length is resolved by at least seven resolution elements and thus prevent artificial fragmentation on the smallest grid scale (Truelove et al. 1997; Robertson & Kravtsov 2008; Ceverino, Dekel & Bournaud 2009). It is effective in the dense ($n > 10 \text{ cm}^{-3}$) and cold ($T < 10^4 \text{ K}$) regions inside galactic disks, while most of the $L\alpha$ emitting gas, which is at temperatures $(1 - 5) \times 10^4 \text{ K}$, is not affected by this pressure floor.

The equation of state remains unchanged at all densities. Stars form in cells where the gas temperature is below 10^4 K and its density is above the threshold $n = 1 \text{ cm}^{-3}$ according to a stochastic model that is roughly consistent with the Kennicutt (1998) law. The ISM is enriched by metals from supernovae type II and type Ia. Metals are assumed to be released from each stellar particle by SNII at a constant rate for 40 Myr since its birth, assuming a Miller & Scalo (1979) IMF and matching the results of Woosley & Weaver (1995). The metal ejection by SNIa assumes an exponentially declining SNIa rate from a

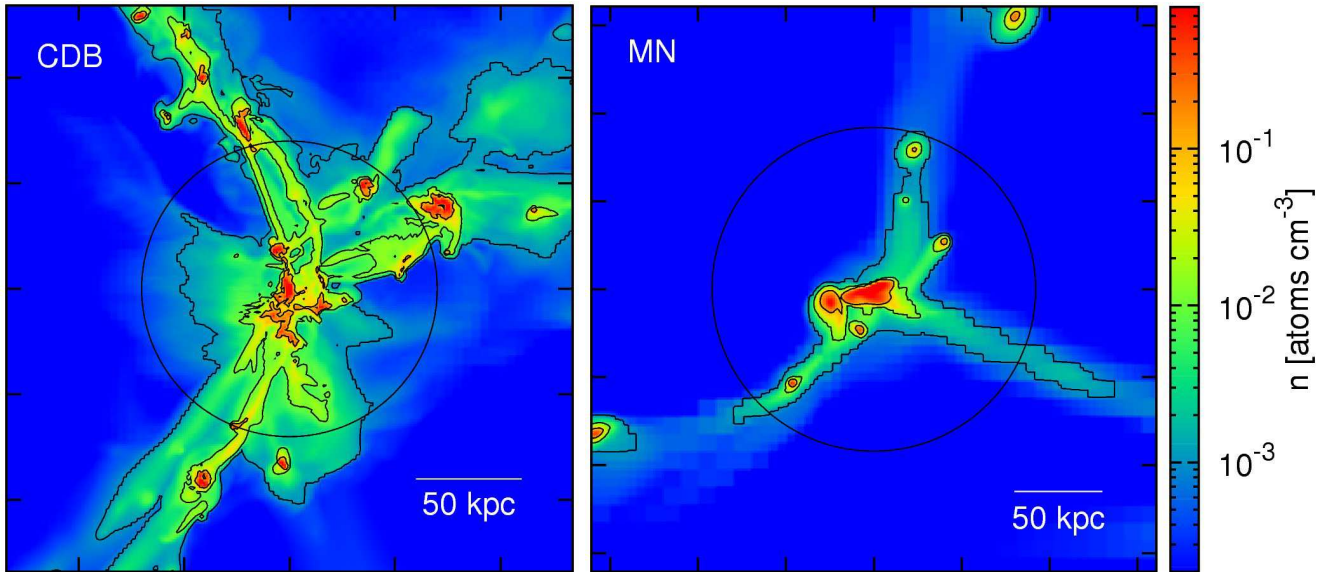


Figure 2. Gas density in simulated galaxies from CDB (left) and MN (right). The colour refers to the maximum density along the line of sight. The contours mark $n = 0.1, 0.01$ and 0.001 cm^{-3} , respectively. The circle shows the virial radius. Left: one of the three CDB galaxies (resolution 70 pc) at $z = 2.3$, with $M_v = 3.5 \times 10^{11} M_\odot$. Right: one of the MN galaxies (resolution 1 kpc) at $z = 2.5$, with $M_v = 10^{12} M_\odot$. In both cases, the inflow is dominated by three cold narrow streams that are partly clumpy. The density in the streams is $n = 0.003 - 0.1 \text{ cm}^{-3}$, with the clump cores reaching $n \sim 1 \text{ cm}^{-3}$.

maximum at 1 Gyr. The code treats the advection of metals self-consistently (Ceverino-Rodriguez 2008).

The dark matter particle mass is $5.5 \times 10^5 M_\odot$, the minimum star particle mass is $10^4 M_\odot$, the smallest cell size is 70 pc (physical units), and the force softening length is 105 pc.

The initial conditions for the CDB simulations were created using a low-resolution cosmological N -body simulation in a comoving box of side $20 h^{-1} \text{ Mpc}$, for which the cosmological parameters were motivated by the WMAP5 following values (Komatsu et al. 2009): $\Omega_m = 0.27$, $\Omega_\Lambda = 0.73$, $\Omega_b = 0.045$, $h = 0.7$ and $\sigma_8 = 0.82$. At $z = 1$, three haloes of $M_v \simeq 10^{12} M_\odot$ each have been selected, avoiding haloes that were subject to a major merger near that time. The three halo masses at $z = 2.3$ are $3.5, 4, 6 \times 10^{11} M_\odot$, and they end up as $(3 - 4) \times 10^{12} M_\odot$ haloes today. For each halo, a concentric sphere of radius twice the virial radius was identified for re-simulation with high resolution. Gas was added to the box following the dark matter distribution with a fraction $f_b = 0.15$. The whole box was then re-simulated, with refined resolution only in the selected volume about the respective galaxy.

3.2 RAMSES Mare Nostrum simulations

The MN simulation uses the AMR code RAMSES (Teyssier 2002). The spatial resolution is $\sim 1 \text{ kpc}$ in physical units. UV heating is included assuming the Haardt & Madau (1996) background model, as in the CDB simulation. The code incorporates a simple model of supernovae feedback and metal enrichment using the implementation described in Dubois & Teyssier (2008). The cooling rates are calculated assuming ionisation equilibrium for H and He, including both collisional- and

photo-ionisation (Katz, Hernquist & Weinberg 1992). Metal cooling is also included using tabulated CLOUDY rates, and is assumed proportional to the metallicity, relative to the Grevesse & Sauval (1998) solar abundances. Unlike in the CDB simulation, no cooling below $T < 10^4 \text{ K}$ is computed, and no self-shielding of the UV flux is assumed. Because we assume that the $\text{Ly}\alpha$ emissions are produced in predominantly shielded gas that is in CIE, our MN computations should be regarded as less accurate than the CDB simulation.

For high-density regions, the MN code considers a polytropic equation of state with $\gamma_0 = 5/3$ to model the complex, multi-phase and turbulent structure of the inter-stellar medium (ISM) (Yepes et al. 1997; Springel & Hernquist 1999) in a simplified form (see Schaye & Dalla Vecchia 1999; Dubois & Teyssier 2008). The ISM is defined as gas with hydrogen density greater than $n_H = 0.1 \text{ cm}^{-3}$, one order of magnitude lower than in the CDB simulation. Star formation has been included, for ISM gas only, by spawning star particles at a rate consistent with the Kennicutt (1998) law derived from local observations of star forming galaxies.

The MN simulation implemented a pressure floor in order to prevent artificial fragmentation, by keeping the Jeans lengthscale, $\lambda_J \propto T n^{-2/3}$, larger than 4 grid-cell sides everywhere. In any case where $n > 0.1 \text{ cm}^{-3}$, a density dependent temperature floor was imposed. It mimics the average thermal and turbulent pressure of the multiphase ISM, in the spirit of Springel & Hernquist (1999) or Dalla Vecchia & Schaye (2008). In our case, we allow the gas to heat up above this temperature floor and cool back. The temperature floor follows a polytropic equation of state with $T_{\text{floor}} = T_0 (n/n_0)^{\gamma_0 - 1}$, where $T_0 = 10^4 \text{ K}$ and $n_0 =$

0.1 atoms cm^{-3} . The resulting pressure floor is given by $P_{\text{floor}} = n_{\text{H}} k_{\text{B}} T_{\text{floor}}$.

We crudely correct for this artificial temperature boost in post-processing by subtracting T_{floor} from the temperature read from the grid cells where $n > 0.1 \text{ cm}^{-3}$. If the corrected temperature is below 10^4 K , we set it to 10^4 K . In practise, almost all cells where $n > 0.1 \text{ cm}^{-3}$ are set to $T = 10^4 \text{ K}$. As will become clear in §4, this means neglecting any $\text{L}\alpha$ emission from these high-density cells. We will evaluate the possible error made by this procedure in the MN galaxies using the more accurate high-resolution CDB galaxies, where no temperature floor has been applied.

For each stellar population, 10% of the mass is assumed to turn into supernovae type II after 10 Myr, where the energy and metals are released in an impulse. For each supernova, 10% of the ejected mass is assumed to be pure metals, with the remaining 90% keeping the metallicity of the star at birth. SNIa feedback has not been considered.

The dark matter particle mass is $1.16 \times 10^7 M_{\odot}$, the star particle mass is $2.05 \times 10^6 M_{\odot}$, the smallest cell size is 1.09 kpc physical, and the force softening length is 1.65 kpc.

The initial conditions of the MN simulation were constructed assuming a Λ CDM universe with $\Omega_{\text{M}} = 0.3$, $\Omega_{\Lambda} = 0.7$, $\Omega_{\text{b}} = 0.045$, $h = 0.7$ and $\sigma_8 = 0.9$ in a periodic box of $50 h^{-1} \text{ Mpc}$. The adaptive-resolution rules in this simulation were the same everywhere, with no zoom-in resimulation of individual galaxies.

4 COMPUTING THE $\text{L}\alpha$ LUMINOSITY

Given the gas temperature T and mass density ρ in every cubic grid cell of the hydrodynamic simulation, we compute the local $\text{L}\alpha$ emissivity produced by electron impact excitation of neutral hydrogen,

$$\epsilon = n_{\text{e}} n_{\text{HI}} q_{1s \rightarrow 2p}(T) h\nu_{\text{L}\alpha} \text{ erg cm}^{-3} \text{ s}^{-1}. \quad (9)$$

In this expression, n_{e} and n_{HI} are the local electron and atomic hydrogen particle densities (in cm^{-3}) and $h\nu_{\text{L}\alpha} = 10.2 \text{ eV} = 1.63 \times 10^{-11} \text{ erg}$ is the $\text{L}\alpha$ photon energy. The temperature dependent quantity $q_{1s \rightarrow 2p}$ is the collisional excitation rate coefficient (Callaway, Unnikrishnan & Oza 1987),

$$q_{1s \rightarrow 2p} = \frac{2.41 \times 10^{-6}}{T^{0.5}} \left(\frac{T}{10^4} \right)^{0.22} \times \exp\left(-\frac{h\nu_{\text{L}\alpha}}{kT}\right) \text{ cm}^3 \text{ s}^{-1}, \quad (10)$$

where T is in degrees K. Radiative recombinations of electrons with protons contribute negligibly to the $\text{L}\alpha$ emissivity, as can be seen from the green, long-dashed curve in Figure 3.

We assume a primordial helium mass fraction $Y = 0.24$, corresponding to a helium particle abundance of 1/12 relative to hydrogen. This gives

$$\rho = (4/3) m_{\text{H}} n_{\text{H}}, \quad (11)$$

where m_{H} is the hydrogen mass and n_{H} is the total density of hydrogen nuclei (neutral plus ionised). The electron and atomic hydrogen densities in eq. (9) are given by

$$n_{\text{HI}}/n_{\text{H}} = x_{\text{HI}} \quad (12)$$

and

$$n_{\text{e}}/n_{\text{H}} = x_{\text{HI}} + (1/12)(x_{\text{HeII}} + 2x_{\text{HeIII}}), \quad (13)$$

where we adopt the temperature dependent ionisation fractions, x_{HI} , x_{HII} , x_{HeII} and x_{HeIII} as computed for collisional ionisation equilibrium (CIE) assuming case-B hydrogen recombination (O. Gnat, private communication; see also Gnat & Sternberg 2007). A large fraction ($\sim 95\%$) of the $\text{L}\alpha$ emission is produced in gas where the helium is fully neutral. In this limit,

$$x_{\text{HI}} = \alpha_{\text{B}}/(\alpha_{\text{B}} + q_{\text{i}}), \quad (14)$$

where α_{B} and q_{i} are the recombination and collisional ionisation rate coefficients (Gnat & Sternberg 2007).

We note for completeness that approximate fits can be provided by

$$\alpha_{\text{B}}(T) = 4.9 \times 10^{-6} T^{-1.5} \left(1 + \frac{115}{T^{0.41}}\right)^{-2.24} \text{ cm}^3 \text{ s}^{-1} \quad (15)$$

and

$$q_{\text{i}} = 21.11 \text{ cm}^3 \text{ s}^{-1} \text{ K}^{3/2} T^{-3/2} \exp\left(-\frac{T_{\text{HI}}}{T}\right) \times \frac{(2T_{\text{HI}}/T)^{-1.089}}{\left[1 + (5.65 T_{\text{HI}}/T)^{0.874}\right]^{1.101}}, \quad (16)$$

with $T_{\text{HI}} = 1.58 \times 10^5 \text{ K}$ being the ionisation threshold according to Hui & Gnedin (1997). We do not use these fits in our calculation here.

We assume that the cold streams are practically *self-shielded* against the photoionising UV background, for the following reason. The typical HI column densities along the shortest dimensions of the streams are $\sim 10^{20} \text{ cm}^{-2}$ and the total hydrogen particle densities are in the range $0.01 - 0.1 \text{ cm}^{-3}$, or typically $\sim 0.03 \text{ cm}^{-3}$ (see Fig. 6). At redshift $z = 3$, the mean Lyman continuum photon intensity is $4\pi J^* \approx 2.2 \times 10^5 \text{ photons s}^{-1} \text{ cm}^{-2}$ (Haardt & Madau 1996) and the unattenuated hydrogen photoionisation rate is $\Gamma = 5.6 \times 10^{-13} \text{ s}^{-1}$. Thus, for gas densities $n \lesssim 2\Gamma/\alpha_{\text{B}} \simeq 4.3 \text{ cm}^{-3}$, the gas will be more than 50% ionised by the unattenuated field. However, absorption of the radiation field in the stream gas will produce a photoionised column

$$N_{\text{HI}}^{\text{photo}} = \frac{2\pi J^*}{n_{\text{H}} \alpha_{\text{B}}} = \frac{4.2 \times 10^{17}}{n_{\text{H}}} \text{ cm}^{-2}. \quad (17)$$

For the typical stream volume densities this is small compared to the neutral columns of $\sim 10^{20} \text{ cm}^{-2}$ that we find, so the streams can be practically assumed to be self-shielded against the background radiation. Parts of the streams may not be self-shielded against local sources of radiation within the streams, e. g. from star-forming satellites. In those case we might overpredict the HI fraction and thus the $\text{L}\alpha$ luminosity.

The CIE neutral hydrogen fraction as a function of temperature and the temperature dependence of the $\text{L}\alpha$ emissivity for a given total density are shown in Fig. 3. One can see that the gas is neutral at $T = 10^4 \text{ K}$ and below, and it becomes highly ionised at $T > 2 \times 10^4 \text{ K}$. The maximum emissivity at a given density is obtained at $T \simeq 1.8 \times 10^4 \text{ K}$, and the emissivity is high enough to substantially contribute to the overall luminosity in the range $T = (1 - 5) \times 10^4 \text{ K}$. Hydrogen in this temperature range is thus the expected source of $\text{L}\alpha$ emission.

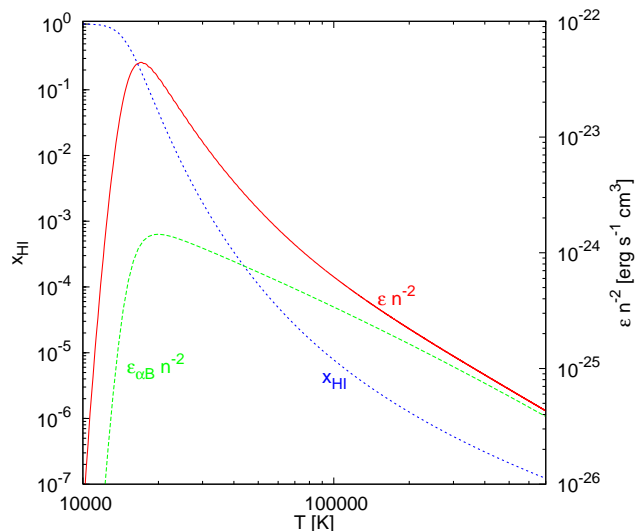


Figure 3. Temperature dependence of the ionisation state and the $\text{Ly}\alpha$ emissivity. The neutral-hydrogen fraction x_{HI} (short-dashed, blue curve) is derived from eq. (14) assuming CIE. The temperature dependence of the emissivity ϵ (solid, red curve) is computed from eqs. (9), (12) and (13) for $n = 1 \text{ cm}^{-3}$. We see that the gas is neutral for $T \leq 10^4 \text{ K}$ and it becomes highly ionised at $T > 2 \times 10^4 \text{ K}$. The maximum emissivity at a given density is obtained at $T \simeq 1.8 \times 10^4 \text{ K}$, and the emissivity is high enough to substantially contribute to an overall luminosity in the range $T = (1 - 5) \times 10^4 \text{ K}$. The contribution of recombination to the emissivity, $\epsilon_{\alpha\text{B}}$ (long-dashed, green curve), is negligible in the relevant temperature range.

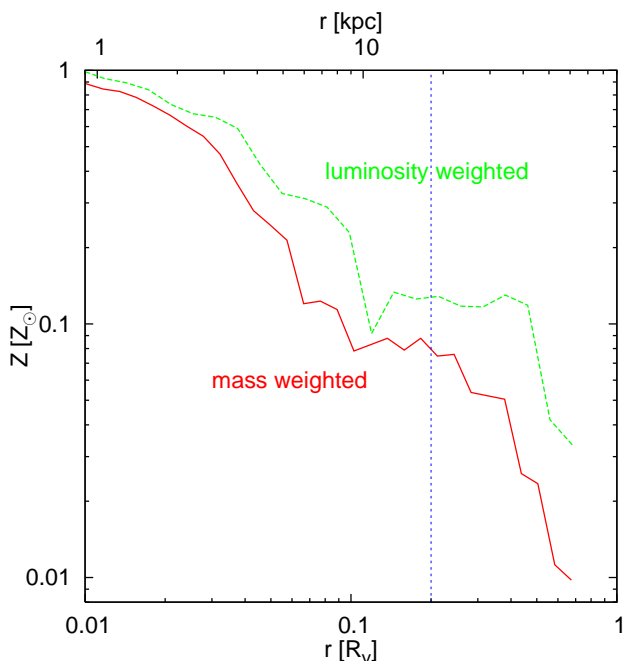


Figure 4. Average metallicity profile in the simulated CDB galaxies, once weighted by the density of the $\text{Ly}\alpha$ emitting cold gas in the temperature range $(1 - 5) \times 10^4 \text{ K}$ and once weighted by the luminosity. The vertical line indicates $0.2 R_v$ which we refer to as the outer border of the galaxy.

The total $\text{Ly}\alpha$ luminosity from a given volume is assumed to be a constant fraction of the sum over all the cells that are contained in that volume,

$$L_{\text{Ly}\alpha} = f_{\alpha} \sum_i \epsilon_i V_i, \quad (18)$$

where V_i is the cell volume. The complex radiation transfer process along the cosmological line of sight is summed up in the transmission factor f_{α} , the fraction of the $\text{Ly}\alpha$ photons that make it to the observer. In §8, we will determine the actual value of f_{α} by matching the predictions from the simulations with a preliminary determination of the observed $\text{Ly}\alpha$ luminosity function. We expect f_{α} to be in the range 0.5-1. This is because the main source of opacity is likely to be intervening and lower redshift intergalactic HI, which is expected to absorb part of the blue side of the line profile. An estimate for a typical line of sight to $z \sim 3$ is $f_{\alpha} \sim 0.85$ (e.g. Faucher-Giguere et al. 2008b). The transmission factor along the line of sight to a typical LAB could be slightly smaller because the LABs tend to reside in overdense environments. A smooth component of HI in the emitting halo may absorb some of the red wing as well. On the other hand, as estimated next, dust opacity is expected to reduce f_{α} by a small factor only except in the galaxy itself and in its immediate vicinity.

Given the gas metallicity in every cell of the simulation, we can estimate the dust absorption as follows. For a medium in which the dust abundance scales linearly with the metallicity Z (with $Z \approx 1$ corresponding to Galactic dust), the continuum opacity due to dust absorption at the $\text{Ly}\alpha$ wavelength is $\tau_{\text{dust}} \simeq 0.1 Z N_{20}$ where N_{20} is the neutral-hydrogen column density in units of 10^{20} cm^{-2} , (Draine 2003). The line optical depth is $\tau_{\text{Ly}\alpha} \simeq 10^7 N_{20} T_4^{-1/2}$ Neufeld (1990) so that $\tau_{\text{dust}} \simeq 10^{-8} Z T_4^{1/2} \tau_{\text{Ly}\alpha}$. For $\text{Ly}\alpha$ scattering through a plane-parallel medium the total line optical depth traversed is $\sim (9 a \tau_0 / \sqrt{\pi})^{1/3} \tau_0$, where τ_0 is the $\text{Ly}\alpha$ optical depth from the mid-plane to the surface, and $a = 4.7 \times 10^{-4} T_4^{-1/2}$ is the damping constant (Adams 1975). Thus, as the photon scatters through the medium the effective dust opacity is

$$\tau_{\text{dust}} \simeq 2.9 Z N_{20}^{4/3} T_4^{-1/3}. \quad (19)$$

For $Z = 0.1$, assuming $T_4 \sim 1$, we obtain $\tau_{\text{dust}} = 1$ for $N_{20} \simeq 3$. We find in the CDB galaxies that the $\text{Ly}\alpha$ luminosity-weighted fraction of volume elements that have a column density $N_{20} \geq 3$ between them and the observer, averaged over different directions, is less than a third. This provides an estimate of no more than a third reduction outside $r \sim 0.1 R_v$ (where $Z \leq 0.1$).

Figure 4 shows the stacked 3D metallicity profile of the $\text{Ly}\alpha$ emitting gas in the three simulated CDB galaxies. It is computed for gas in the temperature range $(1 - 5) \times 10^4 \text{ K}$ and is once weighted by gas density and once by luminosity. The metallicity profiles were computed in spherical shells. The profile shows that the metallicity falls below 0.1 solar outside the disc radius of $\sim 8 \text{ kpc}$, and it drops to much smaller values outside the inner $\sim 30 \text{ kpc}$, where the streams are basically made of compressed intergalactic gas. Therefore dust opacity is estimated to reduce the $\text{Ly}\alpha$ luminosity from the streams by a small factor only. However, this assumption is likely to fail in the inner galactic disk, where the metallicity is above 0.1 solar despite the high

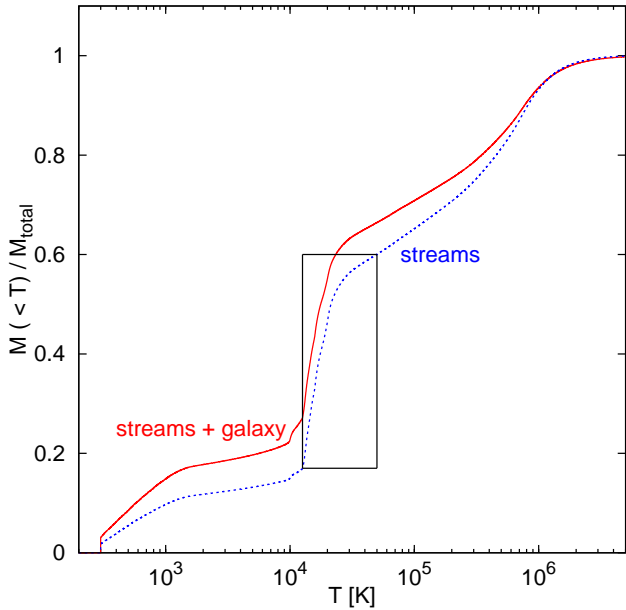


Figure 5. Cumulative, mass-weighted temperature distribution in the stacked 3 CDB haloes at $z = 2.3$. The curves refer to the streams at $r = (0.2 - 1)R_v$ (dashed blue) and to the whole halo including the inner galaxy (solid red). We see that the temperature distribution throughout the halo is bimodal, with cold and hot phases at $10^4 < T < 3 \times 10^4 \text{K}$ and $3 \times 10^5 < T < 2 \times 10^6 \text{K}$, respectively. Outside the inner $0.2R_v$, the hot medium fills the halo while the cold gas is confined to inflowing narrow streams. The cold tail at $T < 10^4 \text{K}$ comes from dense clumps within the streams. The box marks the temperature range of the $L\alpha$ -emitting gas.

redshifts. The effective transmission parameter f_α in the galaxy vicinity is lower than in the streams. By ignoring the dust, we overestimate the $L\alpha$ luminosity from the disk.

5 THE LYMAN-ALPHA EMITTING GAS

Figure 5 shows the cumulative mass-weighted temperature distribution in the CDB galaxies at $z = 2.3$. The distribution is specified alternatively for the halo gas in the radius range $(0.2 - 1.0)R_v$ and for the whole gas, including the inner part that involves the disc and its neighbourhood. We see that the temperature distribution in the halo is bimodal, with a hot virial phase at $10^5 < T < 2 \times 10^6 \text{K}$ containing $\sim 35\%$ of the gas and a cold phase (marked by a box) at $10^4 < T < 3 \times 10^4 \text{K}$ containing $\sim 50\%$ of the gas. A very cold tail at $T < 10^4 \text{K}$ contains $\sim 15\%$ of the gas. For the somewhat more massive MN galaxies, which we do not show here, the situation is qualitatively similar. The temperature distribution is again bimodal, with a hot phase at $6 \times 10^4 < T < 5 \times 10^6 \text{K}$ containing $\sim 45\%$ of the gas and a cold phase at $2 \times 10^4 < T < 4 \times 10^4 \text{K}$ containing $\sim 35\%$ of the gas. An intermediate component in the range $4 \times 10^4 < T < 6 \times 10^4 \text{K}$ contains $\sim 20\%$ of the gas. In the two kinds of simulations, while the hot phase is spread throughout the halo, the cold phase is in the narrow streams flowing through the hot medium and the very cold tail is concentrated in the dense clumps within the streams

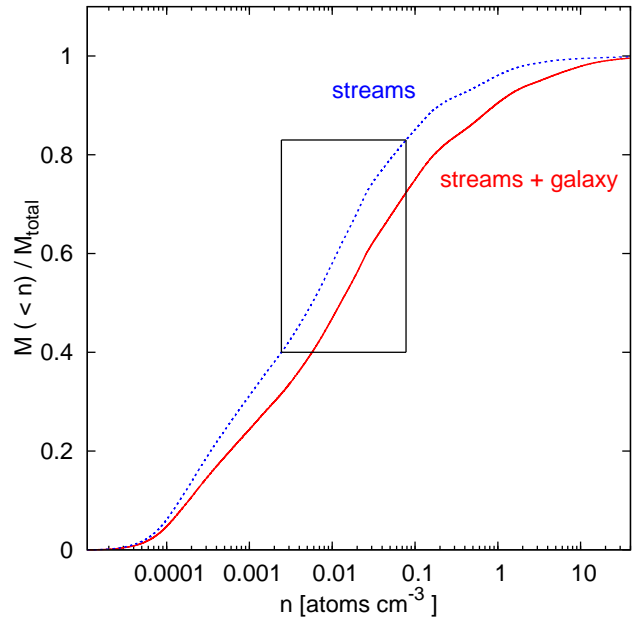


Figure 6. Cumulative, mass-weighted gas density distribution in the stacked 3 CDB haloes at $z = 2.3$. The curves refer to the streams at $r = (0.2 - 1)R_v$ (dashed blue) and to the whole halo including the inner galaxy (solid red). The density in the cold streams is in the range $n = 0.001 - 0.1 \text{cm}^{-3}$, and in the denser colder clumps it becomes $n = 0.1 - 1 \text{cm}^{-3}$. The box marks the density range of the $L\alpha$ -emitting gas, based on the box marked in Fig. 5 and assuming that n is a monotonically decreasing function of T .

and in the disc. Based on the temperature dependence of the emissivity in Fig. 3, we conclude that most of the $L\alpha$ luminosity is expected to come from the cold streams, with about half the total gas mass participating in efficient $L\alpha$ emission.

Figure 6 shows the cumulative mass-weighted gas density distribution in the CDB galaxies at $z = 2.33$ in the same radius zones. If the multi-phase medium is in pressure equilibrium, the rank order of the cells by density and by temperature are exactly opposite of one another, so a comparison of Fig. 5 and Fig. 6 reveals that the $L\alpha$ -emitting cold streams have densities in the range from below 0.01 to above 0.1cm^{-3} (marked by a box). The situation for the MN galaxies is comparable.

Figure 7 shows the two-dimensional gas distribution in the temperature-density plane. It complements Figures 5 and 6 with information on the different gas phases present in the simulations. We see that much of the gas is not in pressure equilibrium, $nT = \text{const}$. The top and bottom panels display the distribution of mass and $L\alpha$ luminosity, respectively. We see that the luminosity peaks at $T = (1 - 2) \times 10^4 \text{K}$ over a broad range of densities from $n = 0.001 \text{cm}^{-3}$ and up. We interpret the $T > 10^4 \text{K}$ gas with densities above $n = 0.1 \text{cm}^{-3}$ outside the central galaxy to be in clumps along the streams. It seems to be associated with a few percent of the mass that contribute about 25% of the luminosity. A similar fraction of the luminosity comes from gas in the temperature range $T = (2 - 7) \times 10^4 \text{K}$.

In order to evaluate the possible error introduced in the

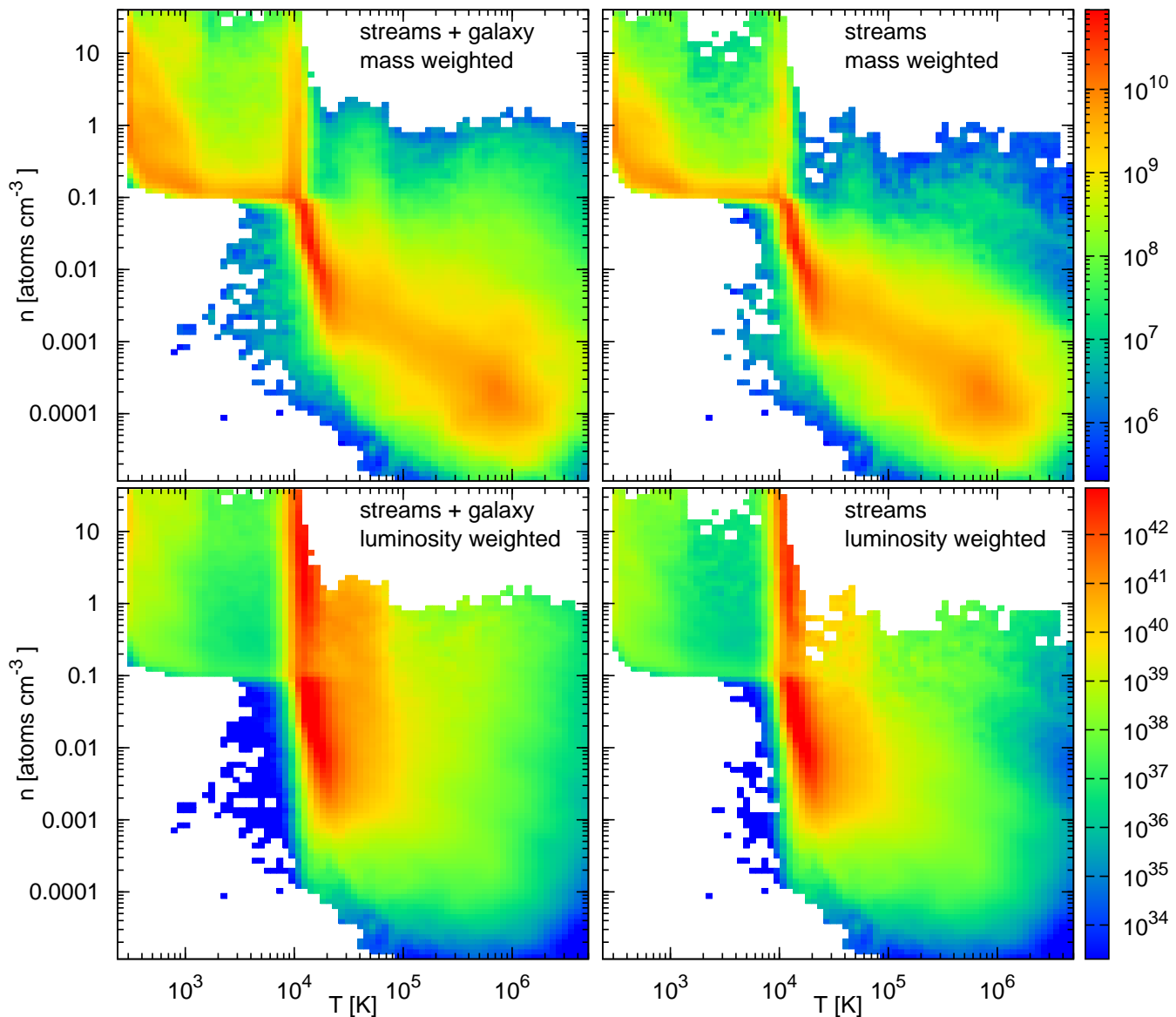


Figure 7. Distribution of mass (top) and luminosity (bottom) in the $n - T$ plane for the stacked 3 CDB haloes at $z = 2.3$. The panels refer to the streams at $r = (0.2 - 1)R_v$ (right) and to the whole halo including the inner galaxy (left). The units are mass M_\odot (top) and erg s^{-1} (bottom) per unit area in the $(\log_{10} n, \log_{10} T)$ plane. The luminosity peaks at $T = (1 - 2) \times 10^4 \text{K}$ over a broad range of densities from $n = 0.001 \text{cm}^{-3}$ and up. Most of the emission is from the streams outside the central galaxy.

MN galaxies by practically ignoring the emissivity from cells with densities $n > 0.1 \text{cm}^{-3}$, we computed the fraction of the luminosity coming from such cells in the CDB galaxies. We find that this fraction is typically only $\sim 15\%$ in the halo at $r > 0.2R_v$, and it could be as high as 40% in the central disc. By adding 15% to the MN emissivities everywhere we obtain a good match between the total luminosities at a given halo mass in the CDB and MN simulations (see Fig. 12).

6 SIMULATED LYMAN-ALPHA BLOBS

Figures 8 and 9 show sample images of simulated galaxies, two CDB galaxies and two MN galaxies. The haloes are of

virial mass $M_v \simeq 4 \times 10^{11}$ and $10^{12} M_\odot$ respectively, and the corresponding redshifts are $z = 2.3$ and 2.5.

The top panels present the neutral hydrogen column density as computed in §4 assuming CIE. The middle panels are maps of $\text{L}\alpha$ restframe surface brightness S , namely a fraction f_α of the emissivity integrated along the line of sight, as emitted per unit area at the galaxy. The bottom panels show images of “observed” surface brightness I as an observer would see it, per unit area in the galaxy and at the telescope. The restframe surface brightness is converted to observed surface brightness via

$$I = \frac{S}{4\pi(1+z)^4}, \quad (20)$$

In order to obtain realistic images, we applied a Gaussian

PSF with a 0.6 arcsec FWHM to mimic atmospheric distortions in good seeing conditions, and assumed a pixel size of 0.2 arcsec at the telescope.

One can read from the middle maps the fraction of the luminosity that comes from each of the different parts of the halo. In particular, we consider separately (a) the contribution from the disc galaxy and its near vicinity inside a circle of radius $0.2R_v$ and (b) the contribution from the halo at $0.2 - 1.0R_v$. We see in the figure that the restframe surface brightness in the inner galaxy reaches values higher than $S \sim 10^{40} \text{ erg s}^{-1} \text{ kpc}^{-2}$ but over a limited area of $\sim 10^2 \text{ kpc}^2$, thus contributing $L \sim$ a few $\times 10^{42} \text{ erg s}^{-1}$. The typical surface brightnesses in the halo are lower by a factor of a few, but the emission regions are spread over an area that is larger by an order of magnitude, thus providing a comparable contribution to the total luminosity. Most of the luminosity comes from the low-density streams, and a non-negligible fraction is from clumps associated with the streams.

Recall that the emission from the disc may be partly absorbed by dust, which is ignored here, but we do not expect substantial dust absorption in the streams in the outer halo, where the metallicity is 0.01 to 0.1 solar. We can thus consider the halo contribution to be a safe lower limit to the overall $L\alpha$ luminosity, and take the luminosity as estimated from the whole system of disc plus halo as an upper limit.

In the bottom panels we see blobs with surface brightness above $10^{-18} \text{ erg s}^{-1} \text{ cm}^{-2} \text{ arcsec}^{-2}$ extending to $\sim 100 \text{ kpc}$. The images are clumpy and irregular. Their shapes are non-circular; they tend to be elongated and asymmetric, showing finger-like extensions. These sample images resemble the observed images of LABs, e.g., those shown in Figure 8 of Matsuda et al. (2004). Figure 10 compares “observed” surface brightness maps of two simulated CDB galaxies (from the bottom panels of Figures 8 and 9) with the images of the two most luminous LABs observed by Matsuda et al. (2004). The qualitative similarity of the irregular, clumpy and elongated LAB morphologies and their sizes is encouraging.

7 LYMAN-ALPHA LUMINOSITY AS A FUNCTION OF MASS AND REDSHIFT

The variation of average total $L\alpha$ luminosity from within the virial sphere as a function of halo mass and redshift, as derived from the simulations, is shown in Fig. 11. The two panels refer to the luminosity from the whole halo, streams and central galaxy, as an upper limit, and to the streams at $r > 0.2R_v$ only as a lower limit. The fraction of the radiation emitted is set to $f_\alpha = 0.85$, as determined by a fit to the observed luminosity function in §8 below. The luminosities are quoted for small bins about points in the (M_v, z) plane. Four points refer to the average luminosities over the three CDB galaxies at $z = 1.9, 2.5, 3.2$ and 4.0 . Each of the other points refer to the average over 12 MN galaxies. The two-dimensional functional fit to the quoted values, $L(M_v, z)$, is shown in colours. We use a function of the form

$$L_{43}(M_v) = A (M_{12})^B (1+z)^C, \quad (21)$$

where A , B and C are free parameters, $L_{43} \equiv L_{L\alpha}/10^{43} \text{ erg s}^{-1}$ and $M_{12} \equiv M_v/10^{12} M_\odot$. To determine the free parameters, we first address the mass dependence at a fixed redshift where we have performed our most detailed analysis in CDB, $z \simeq 2.4$. We then assume that the same mass dependence is valid between $z \sim 2$ and $z \sim 4$, and evaluate the redshift dependence.

Figure 12 shows the luminosity as a function of halo mass at $z = 3.1$. The luminosity is computed within the isophotal surface brightness threshold of $2.2 \times 10^{-18} \text{ erg s}^{-1} \text{ cm}^{-2} \text{ arcsec}^{-2}$, also used by Matsuda et al. (2004). We adopted $f_\alpha = 0.85$. A small correction upward of $\sim 30\%$ has been applied to the results as extracted at $z \simeq 2.4$ in order to bring them to $z = 3.1$ in this plot, using eq. (21) with $C = 1.3$ as determined below. The average luminosity for the three CDB galaxies is shown at $M_v \simeq 4 \times 10^{11} M_\odot$. Each of the other symbols is the average of 12 MN galaxies. We see that in the mass range most relevant for LABs, $M_v = 10^{11.5} - 10^{12.5} M_\odot$, the luminosity is roughly proportional to halo mass. This dependence is driven by the near-linear mass dependence of the accretion rate, eq. (5).

For a more accurate description of the mass dependence we fit the function of eq. (21) to the results at the fixed redshift $z \simeq 2.4$, using least-squares fit in the log, and obtain the lines shown in Fig. 12 with $B = 0.80$ for the whole halo and $B = 0.76$ for the streams only.

We next use this functional mass dependence to scale the simulated results at other redshifts to a fixed mass, $M_v = 10^{12} M_\odot$. The results are the values as quoted in the (M_v, z) bins shown in Fig. 11. The scaled luminosities are shown in Fig. 13. A crude power-law fit to the symbols yields a redshift-dependence power index $C = 1.3$, with the normalisation parameters $A = 0.188$ and 0.0972 for streams+galaxy and for streams only, respectively. We note that the obtained redshift dependence of the luminosity is somewhat weaker than the $(1+z)^{2.2}$ dependence of the accretion rate in eq. (5). The accuracy of this scaling with redshift is not an important issue for us here since we only use it to correct the luminosities from $z \simeq 2.4$ to $z = 3.1$, a correction of less than 30%.

8 LYMAN-ALPHA LUMINOSITY FUNCTION

To obtain a predicted LAB luminosity function at $z \sim 3$, we convolve $L_{L\alpha}(M_v)$ with the Sheth-Tormen halo mass function (Sheth & Tormen 1999) at the same redshift. Here we assume a cosmology with $\Omega_\Lambda = 0.72$, $\Omega_M = 0.28$, $\sigma_8 = 0.83$, $h = 0.71$ and $\Omega_B = 0.045$. The resultant luminosity function is presented in Fig. 14, both for the total luminosity within the virial radius and for the halo streams only, in the range $0.2 - 1.0R_v$, which we consider to be upper and lower limits respectively given the uncertainty in the dust obscuration from the inner galaxy. The fraction of emitted radiation, which could range in principle between 0.5 and 1.0, is set to $f_\alpha = 0.85$.

We computed a crude estimate of the observed $L\alpha$ luminosity function at $z \sim 3.1$ in 3 luminosity bins using the most recent 201 LABs observed by Matsuda et al. (private communication). This sample contains three fields of different environment densities, and can thus be crudely considered as a fair sample. The number densities

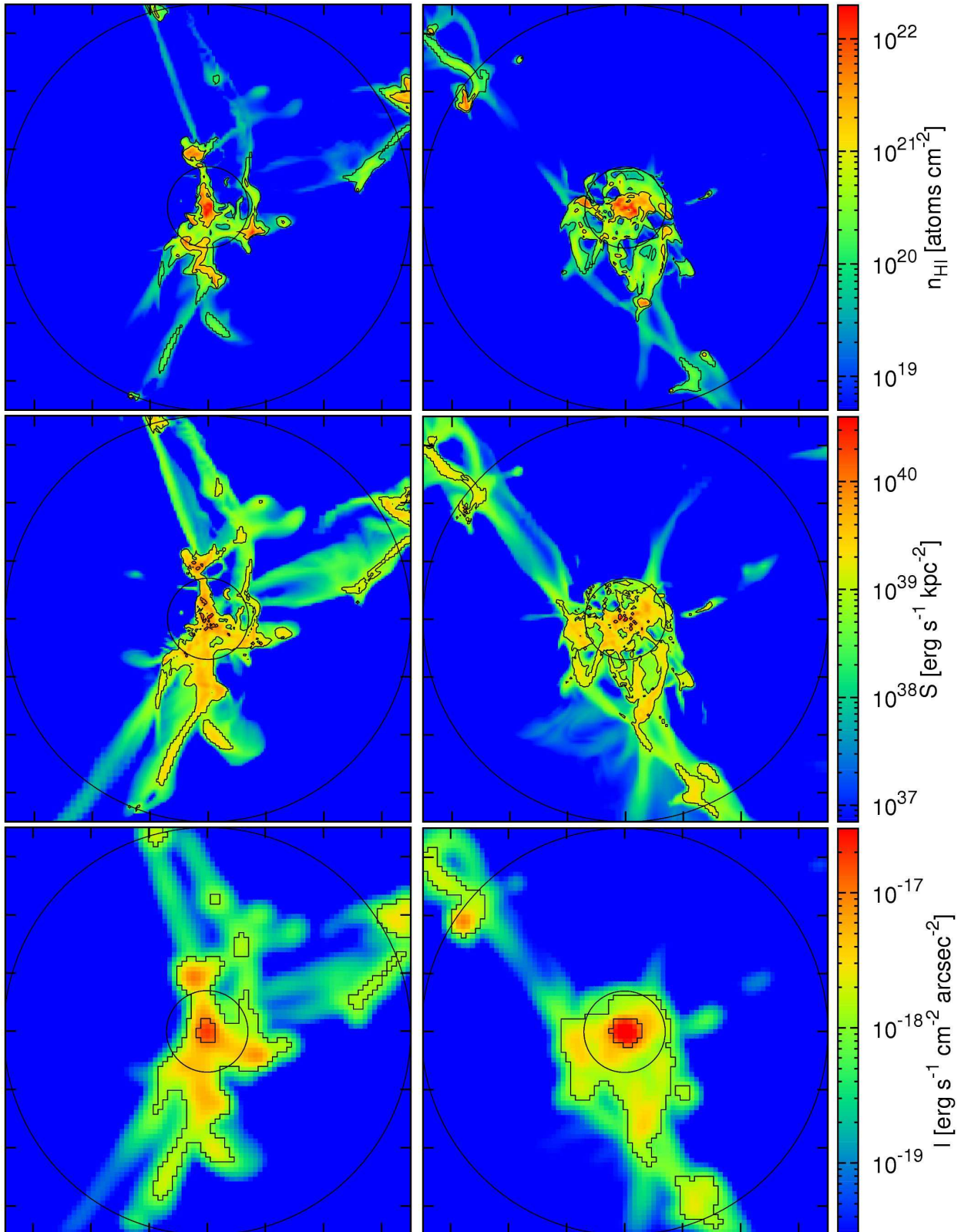


Figure 8. Images of two simulated CDB galaxies at $z = 2.3$ (left and right). The virial masses are $M_v \simeq 4 \times 10^{11} M_\odot$. The box side is 140 kpc (physical). The outer circle marks the virial radius and the inner circle is at $0.2R_v$. Top: Neutral-hydrogen column density. Contours are shown for 10^{20} and 10^{21} cm^{-2} . Middle: Restframe surface brightness S , with $f_\alpha = 0.85$, showing contours at 10^{39} and $10^{40} \text{ erg s}^{-1} \text{ kpc}^{-2}$. Bottom: “Observed” surface brightness I , at an angular resolution of $\sim 0.1 \text{ arcsec}$, with contours at 10^{-18} and $10^{-17} \text{ erg s}^{-1} \text{ cm}^{-2} \text{ arcsec}^{-2}$, corresponding to the contours of S . The fraction of luminosity that originates from within these contours is 80% and 20%, respectively.

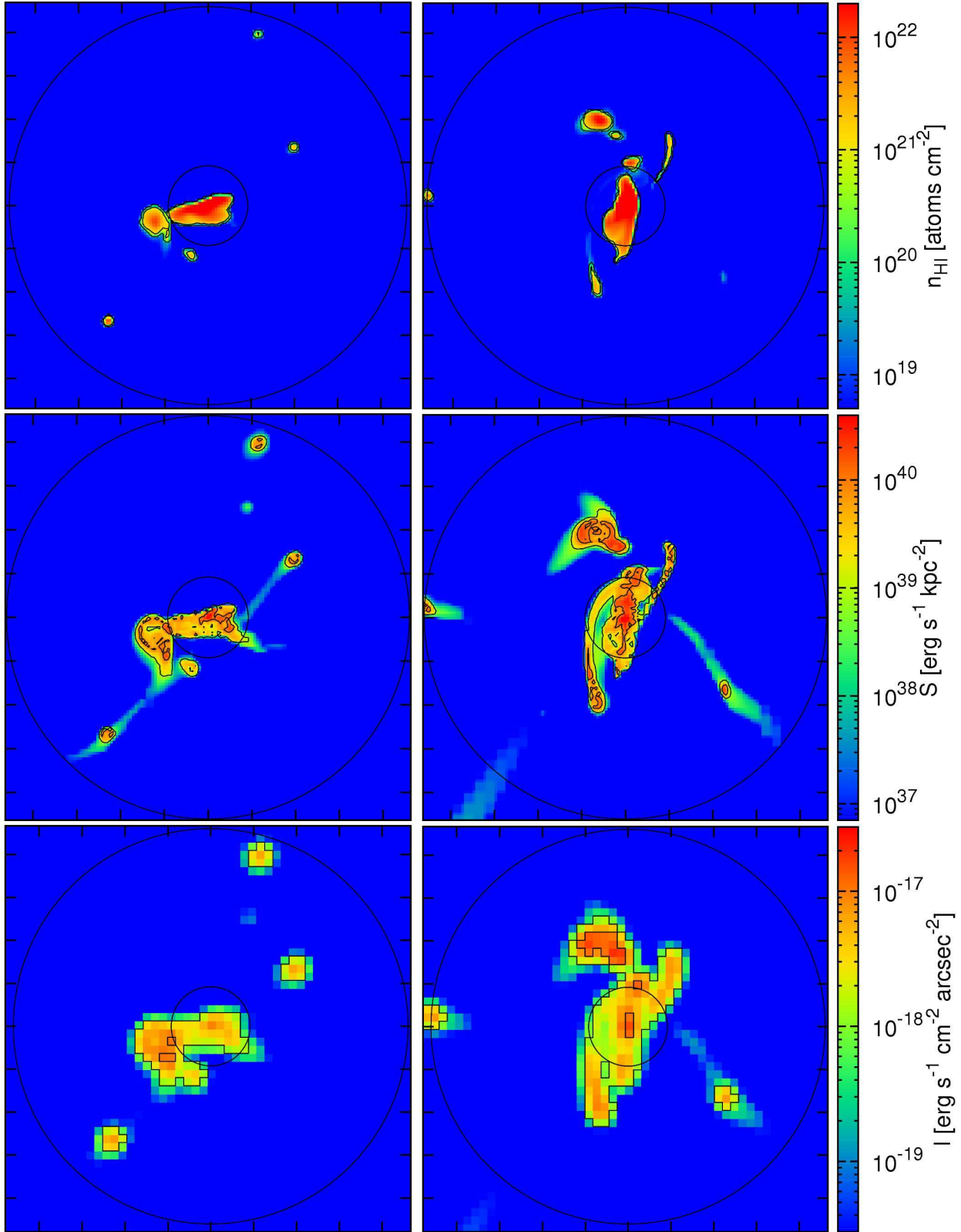


Figure 9. Images of two simulated MN galaxies at $z = 2.5$ (left and right). The virial masses are $M_v \simeq 10^{12} M_\odot$. The box side is 184 kpc (physical). The outer circle marks the virial radius and the inner circle is at $0.2R_v$. Top: Neutral-hydrogen column density. Contours are shown for 10^{20} and 10^{21} cm^{-2} . Middle: Restframe surface brightness S , with $f_\alpha = 0.85$, showing contours at 10^{39} and $10^{40} \text{ erg s}^{-1} \text{ kpc}^{-2}$. Bottom: “Observed” surface brightness I , at an angular resolution of $\sim 0.1 \text{ arcsec}$, with contours at 10^{-18} and $10^{-17} \text{ erg s}^{-1} \text{ cm}^{-2} \text{ arcsec}^{-2}$, corresponding to the contours of S . The fraction of luminosity that originates from within these contours is 93% and 18%, respectively.

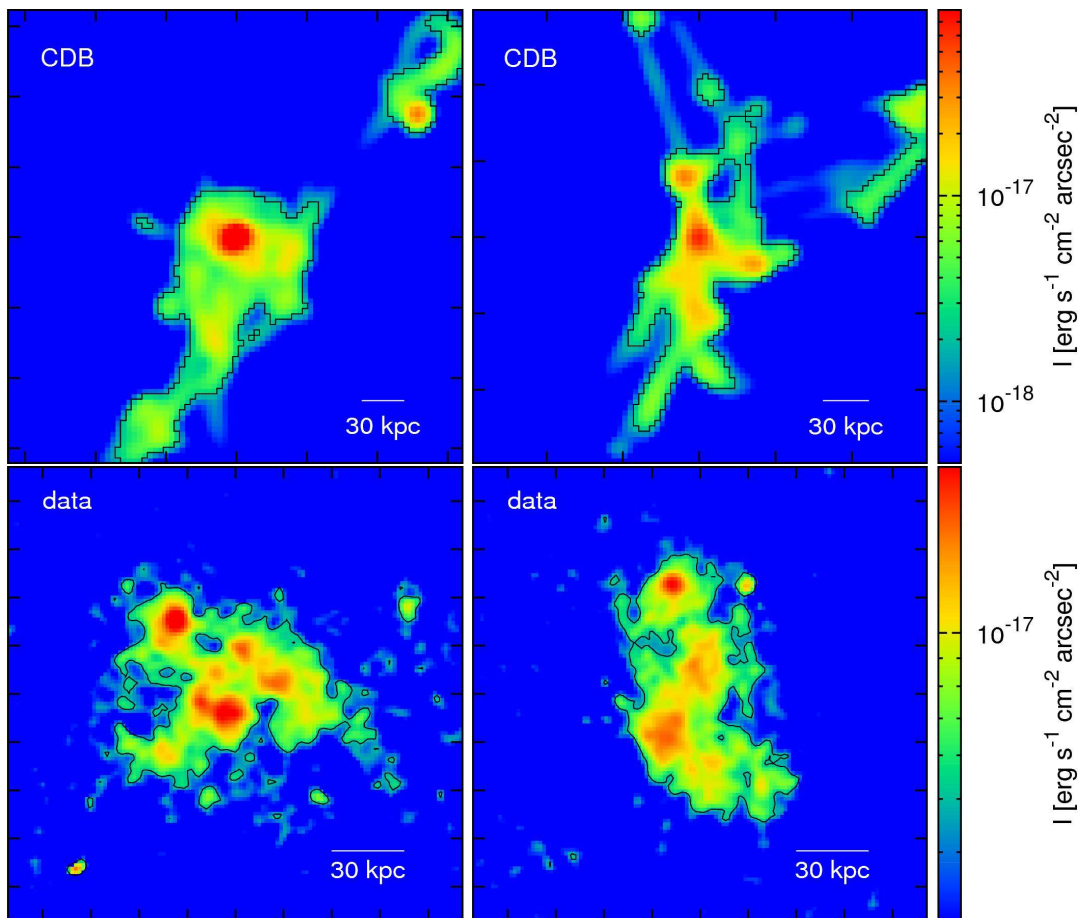


Figure 10. A qualitative crude comparison of images of simulated (top) and observed (bottom) LABs. The observed LABs are the two most luminous LABs from Matsuda et al. (2004) with $L \simeq 10^{44}$ erg s $^{-1}$. The simulated images are of CDB galaxies scaled from $z = 2.3$ to $z = 3.1$ and to the luminosity of the corresponding observed LABs using $I \propto R \propto L^{1/3}$ (the original, unscaled luminosity was 5×10^{43} erg s $^{-1}$). All four maps have an angular resolution of ~ 0.2 arcsec.

were determined by counting the number of blobs in the luminosity bins and dividing by the comoving survey volume of $V_s = 1.5 \times 10^6$ Mpc 3 (or physical volume 3.6×10^5 Mpc 3). Also shown is the luminosity function derived earlier from a partial sample of 35 LABs in a dense cluster environment (Matsuda et al. 2004) 3 . The latter overestimates the universal luminosity function by a factor of a few as expected from the high environment density. A Poissonian error has been attached to every bin. The number

3 The comoving survey volume here is $V_s = 1.3 \times 10^5$ Mpc 3 (or physical volume 3.2×10^4 Mpc 3). They used a cosmology with $\Omega_M = 0.3$, $\Omega_\Lambda = 0.7$ and $h = 0.7$, which is very close to the cosmologies used in the simulations and in the analysis. They choose their sample as explained in their section 3. The observed luminosity function was computed for a combined limit of surface brightness (2.2×10^{-18} erg s $^{-1}$ arcsec $^{-2}$) and size (16 arcsec $^{-2}$), while in the simulations we use only a surface brightness limit. Had we imposed a similar size limit in the simulations, one can deduce from Fig. 16 that our predicted luminosity function would have been suppressed at luminosities below a few times 10^{42} erg s $^{-1}$, making the comparison with the counts at the faint end less certain.

density has been derived by dividing the number of objects in each bin by the total survey volume.

We learn from Fig. 14 that the predicted luminosity function has a similar slope to the observed one. For $f_\alpha \sim 0.85$, the predicted upper and lower limits border the observed function from above and below throughout the whole range of LAB luminosities. We find that f_α changes roughly linearly with the adopted cosmological σ_8 through its effect on $n(M)$. Therefore, the $\sim 10\%$ uncertainty in σ_8 translates into a similar uncertainty in f_α .

Also shown is the luminosity function as estimated from our crude toy model for gravitational heating, §2, again convolved with the Sheth-Tormen halo mass function, and using $f_\alpha f_c = 0.34$. It is remarkable that this very crude toy model recovers the simulation results in the relevant mass range to within a factor of a few.

9 SURFACE-BRIGHTNESS PROFILE, AREA AND LINEWIDTH

A detailed comparison of theory to data will be presented in a future paper where we apply a more accurate radiative transfer calculation to the simulated galaxies. However, it is

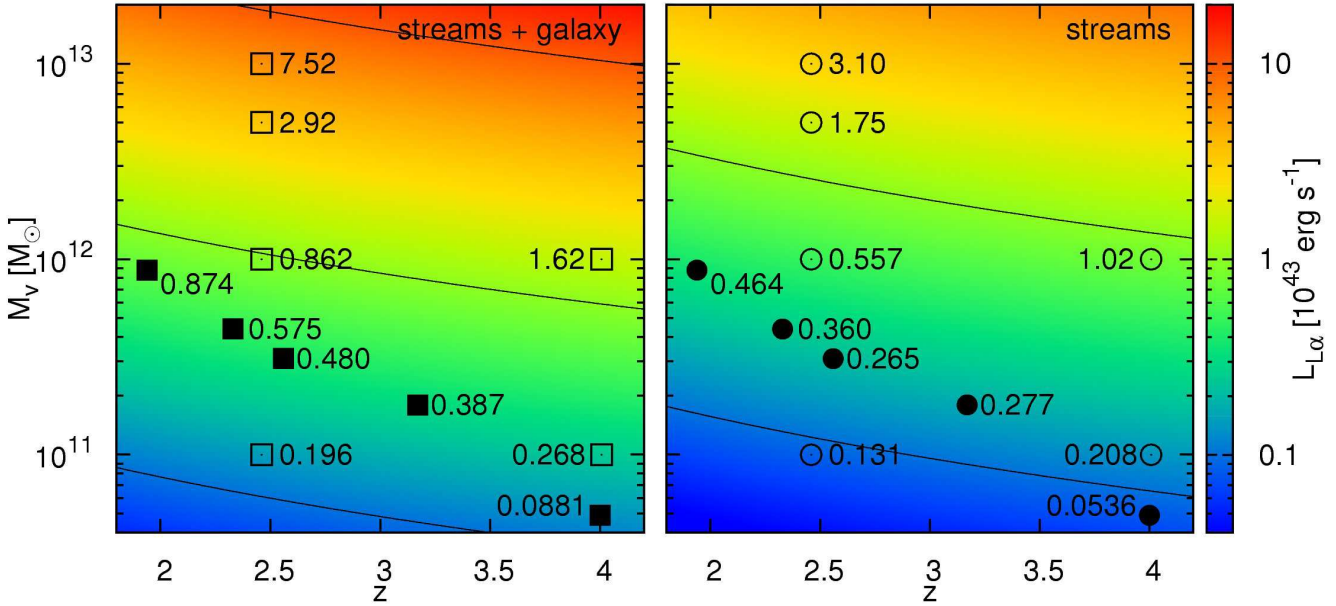


Figure 11. Total $L\alpha$ luminosity as a function of halo mass and redshift, separately for streams+galaxy (*left*) and for streams only (*right*). The average values as drawn from the simulations in bins of (M_v, z) are marked by symbols and numbers in units of $10^{43} \text{ erg s}^{-1}$. The CDB results are marked by filled symbols and the MN results by open symbols. Shown in colour is the fitting function eq. (21) with contours at 10^{42} , 10^{43} and $10^{44} \text{ erg s}^{-1}$.

worthwhile to report here on a preliminary comparison with data, based on the simplified analysis of the current paper, which is encouraging.

9.1 Surface-brightness profile

Figure 15 shows the surface-brightness profile of the stacked images from the three CDB simulations, assuming $f_\alpha = 0.85$ throughout the whole halo. It is compared to stacked profiles of 35 observed LABs from Matsuda et al. (2004). For the stacking of the observed LABs, which range over more than an order of magnitude in luminosity, we scale the LAB radius R and surface brightness I to a fiducial luminosity $L_0 = 10^{43} \text{ erg s}^{-1}$. We write $L \propto I R^2$ and assume $L \propto M_v$ and $R \propto R_v \propto M_v^{1/3}$ to obtain the scaling $R \propto I \propto L^{1/3}$. Thus, for a LAB with luminosity L , we multiply both the radius and the surface-brightness by the factor $(L_0/L)^{1/3}$. Non-zero values for I are considered for each LAB only above the isophotal surface-brightness threshold of $2.2 \times 10^{-18} \text{ erg s}^{-1} \text{ cm}^{-2} \text{ arcsec}^{-2}$ and only the inner adjacent non-zero values (i.e. all values outside the innermost zero value are also treated as zero values) were used in the averaging of I at each radius r . The stacked simulated profile has been scaled accordingly to match the same fiducial luminosity L_0 .

We see that a power law $I(r) \propto r^{-\gamma}$ is a good fit to the simulated profile, with $\gamma \simeq 1.2$, from the disk scale $r < 10$ kpc out to ~ 40 kpc, which is about half the virial radius. It seems to steepen to $\gamma \sim 2$ at larger radii.⁴ The observed images of Matsuda et al. (2004) are subject to a point spread function of ~ 1 arcsec, which is responsible for the flattening

⁴ Note that the slope $\gamma \simeq 1.2$ is consistent with the slope of the cumulative 3D luminosity profile shown in Fig. 1, where $L(< r) \propto r^{0.8}$ in the range $r = (0.1 - 0.4) R_v$.

of the observed profile at $r \leq 10$ kpc. Given the high background outside the surface-brightness threshold, the meaningful part of the observed stacked profile is limited to the range 10 – 30 kpc. In this range, the power law with a slope $\gamma = 1.2$ provides a good fit to the observed profile as well. We also see that the crude toy model of §2 provides a profile that is consistent with the simulated profile to within a factor of two, as seen in Figure 1.

9.2 Isophotal area

Two of the observable global quantities for each LAB are the area encompassed by an isophotal contour of a given threshold surface brightness, and the corresponding luminosity. In order to compare to the data of Matsuda et al. (2004), we applied to our simulated galaxies, scaled to $z = 3.1$, a threshold of $2.2 \times 10^{-18} \text{ erg s}^{-1} \text{ cm}^{-2} \text{ arcsec}^{-2}$.

Figure 16 displays the areas and luminosities of our simulated LABs in comparison with the 35 observed LABs. Each of the three simulated CDB galaxies is “observed” from three orthogonal directions, and each of the randomly selected MN galaxies is “observed” from one random direction. We see that the area at a given luminosity in MN is systematically smaller than in CDB, but only by a factor of two. The simulations agree with the observations to within a factor of two, and they reproduce the general correlation between area and luminosity. The overall trend follows the scaling relation

$$A \propto L^{0.75}. \quad (22)$$

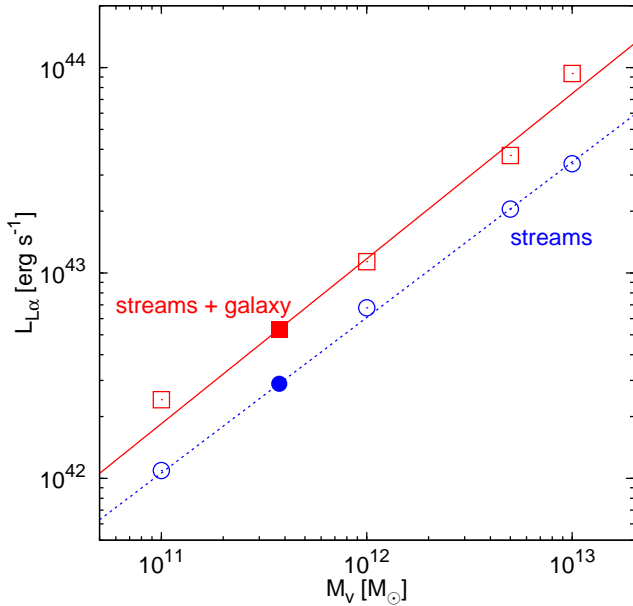


Figure 12. L_{α} luminosity as a function of halo mass at $z = 3.1$ with $f_{\alpha} = 0.85$, for the total luminosity within the virial radius (upper, red symbols and curve), and for the halo outside $0.2R_v$ (lower, blue symbols and curve). Each symbol represents the average luminosity over simulated haloes of a given mass, 12 haloes from the MN simulation (open symbols) and 3 from the CDB simulations (filled symbols). The lines are least-squares fits using eq. (21) with slopes $B = 0.80$ and 0.76 , respectively.

9.3 Linewidth

The major contribution to the LAB line profile is the kinematic effect owing to the distribution of line-of-sight velocities in the cold gas. It is dominated by the coherent instreaming velocities from the background and from the foreground, corresponding to a FWHM of order a few times the halo virial velocity. The effect of resonant scattering of L_{α} should be convolved with the kinematic effect.

In Fig. 17 we show the kinematic components of three characteristic line profiles from the simulated CDB galaxies. The effect of resonant scattering is not included yet. For any desired direction of view, the kinematic line profile is computed as the luminosity weighted distribution of the line-of-sight velocities across the whole isophotal area. In some cases, the line profile is dominated by one peak, corresponding to a stream that stretches roughly along the line of sight. In other cases, the line profile is bimodal, with a red peak and a blue peak corresponding to two opposite streams that lie not far from the line of sight. A third type of line profile is flatter, showing three peaks, the central of which corresponding to a stream that is roughly perpendicular to the line of sight. We crudely estimate the kinematic FWHM as twice the standard deviation of Δv .

Resonant scattering of the L_{α} photons in the stream neutral hydrogen gas broadens the L_{α} emission line profile as the trapped photons diffuse into the damping wings before finally escaping (Adams 1972; Neufeld 1990). For scattering and escape from a static plane parallel medium, the total line width, in units of the Doppler parameter, is (Adams 1972; Harrington 1973)

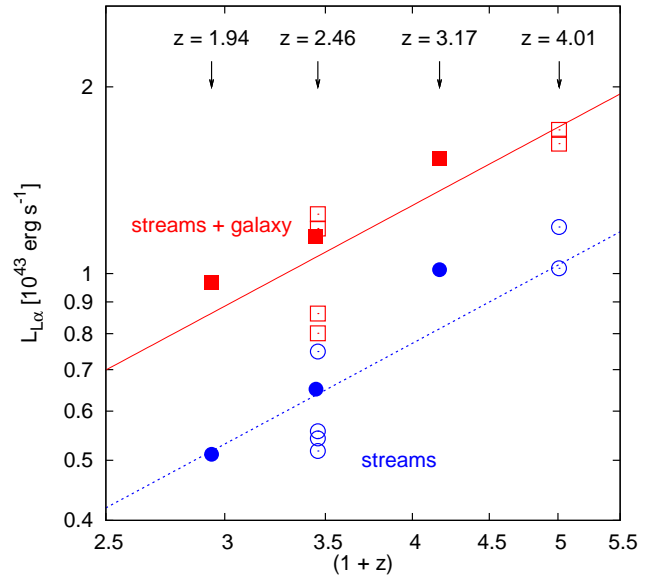


Figure 13. L_{α} luminosity as a function redshift for $M_v = 10^{12} M_{\odot}$ with $f_{\alpha} = 0.85$, for the total luminosity within the virial radius (upper, red symbols and curve), and for the halo outside $0.2R_v$ (lower, blue symbols and curve). Each symbol represents the average luminosity over simulated haloes of a given mass, 12 haloes from the MN simulation (filled symbols) and 3 from the CDB simulations (open symbols). The luminosities were scaled from the simulated values at the different halo masses to $M_v = 10^{12} M_{\odot}$ using the mass dependence obtained in eq. (21). The curves are approximate eye-ball power-law fits with a slope $C = 1.3$.

$$\sigma_{\text{scat}} \simeq 2[a \tau_{L\alpha} \sqrt{(3/\pi)}]^{1/3}. \quad (23)$$

For L_{α} , the Doppler parameter is $b = 12.89 T_4^{1/2} \text{ km s}^{-1}$, and the radiation parameter a and the optical depth $\tau_{L\alpha}$ are given in §4 following eq. (19). We obtain

$$\sigma_{\text{scat}} \simeq 436 N_{20}^{1/3} T_4^{1/6} \text{ km s}^{-1}. \quad (24)$$

Thus, the line profile resulting from resonant scattering of a midplane source is expected to consist of a red and a blue peak separated by σ_{scat} . For a very crude estimate of total line width Δv , we add in quadrature σ_{scat} to the FWHM of the kinematic line profile.⁵

Figure 18 displays isophotal area versus linewidth for the simulated LABs and for observed L_{α} emitters Matsuda et al. (2006), including LABs and less extended emitters. The simulations and observations show a similar general trend, which very crudely follows $A \propto (\Delta v)^{2.25}$, but the data show large scatter. A comparison to the tighter correlation seen in Fig. 16 between the area and the luminosity indicates that the scatter in Fig. 18 is mostly due to scatter in Δv . This scatter is partly due to the variations in the relative orientations of the streams and the line of sight. The spread in the Δv as estimated in the simulations is underestimated due to the fact that we added in quadrature a constant value of $\sigma_{\text{scat}} = 436 \text{ km s}^{-1}$. This

⁵ We note that the effect of resonant scattering as determined for a static medium may be an overestimate because of turbulent motions.

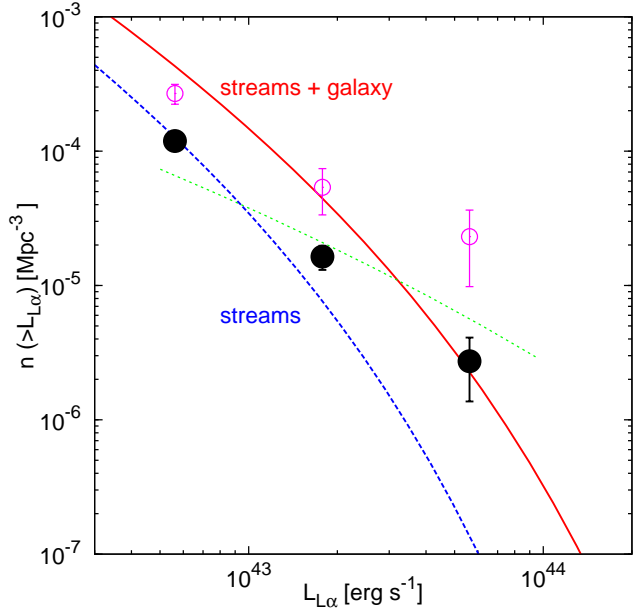


Figure 14. $L\alpha$ luminosity function, showing the comoving number density of LABs brighter than $L_{L\alpha}$ at $z = 3.1$. The observed symbols (black, filled circles) are based on a sample of 201 LABs by Matsuda (private communication) in a fair sample. The earlier, higher estimates (magenta, open circles) are based on 35 LABs in a dense cluster environment. The lower and upper limits for the luminosity function as derived from the simulations are shown, for streams only (dashed, blue curve) and for streams+galaxy (solid, red curve), respectively. The transmission factor was set to $f_\alpha = 0.85$ for a best match between theory and observation. The gravitational-heating toy-model prediction based on eq. (7) is shown (green, dashed line).

is also responsible for the artificially sharp lower bound at $\Delta v = 436 \text{ km s}^{-1}$, which is apparent for small values of A .

Finally, Fig. 19 displays linewidth versus luminosity for the simulations and a subset of the observed LABs by Matsuda et al. (2006). The simulations reveal a scaling relation that can be approximated by $\Delta v \propto L^{0.18}$. The simulations and observations agree to within a factor better than two, but the larger scatter in the observed data confirms our suspicion that we have underestimated the scatter in the analysis of Δv from the simulations.

We conclude that our simplified analysis of $L\alpha$ emission from simulated galaxies qualitatively reproduces the observed correlations between the global quantities of $L\alpha$ luminosity, area and linewidth. A more detailed comparison of theory and observed LABs, especially involving line profiles and linewidths, should await a more accurate analysis of the simulations using radiative transfer and including dust absorption, as well as photometric and spectroscopic measurements of a larger sample of observed LABs.

10 GRAVITATIONAL HEATING

We now return to the energy source for the $L\alpha$ emission in our simulations. In addition to the gravitational

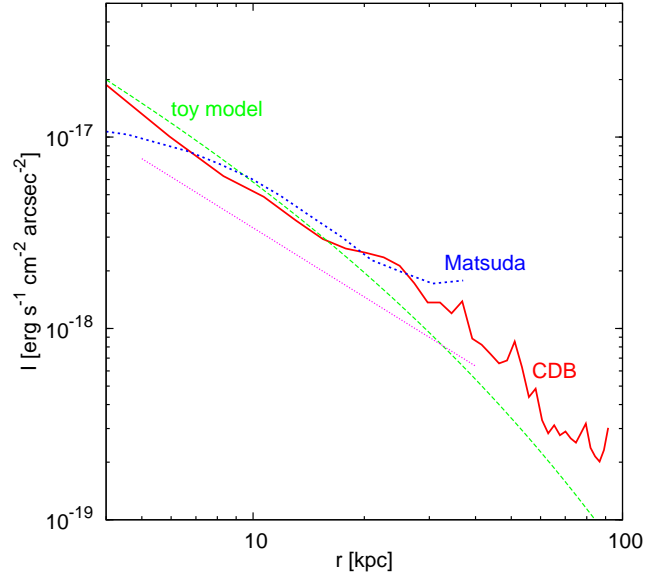


Figure 15. $L\alpha$ surface-brightness profile. The stacked profile from the three CDB galaxies (red, solid line) scaled from $z = 2.3$ to $z = 3.1$ is compared to the stacked profile of 35 observed LABs from Matsuda et al. (2004) at $z = 3.1$ (blue, dotted curve). The individual profiles are scaled to a LAB of a fiducial luminosity of $10^{43} \text{ erg s}^{-1}$ (see text). The toy-model prediction from section 2 is shown (green, dashed curve). A power law of slope -1.2 is shown as a reference (pink, dotted line). There is a good agreement between simulation and data in the radius range $10 - 30 \text{ kpc}$, where the observed profile is meaningful.

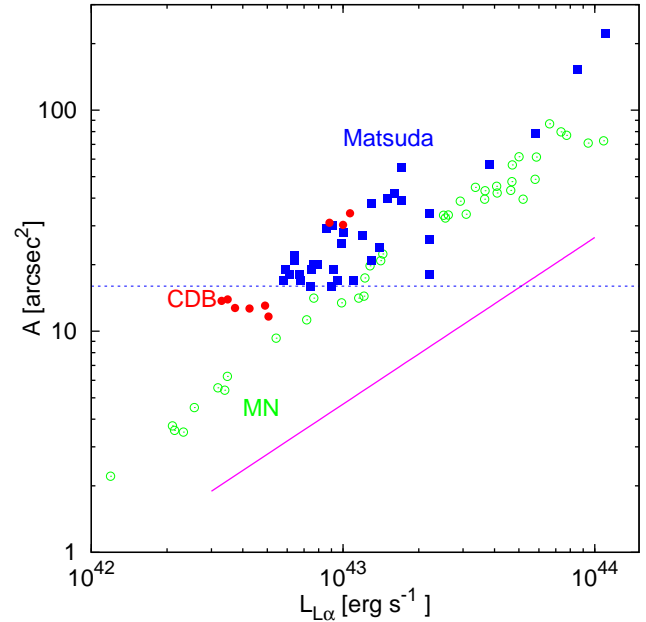


Figure 16. Isophotal area versus luminosity of LABs at $z = 3.1$, above a surface-brightness threshold of $2.2 \times 10^{-18} \text{ erg s}^{-1} \text{ cm}^{-2} \text{ arcsec}^{-2}$. The simulated LABs from CDB (red filled circles) and MN (green open circles) are compared with the 35 observed LABs from Matsuda et al. (2004) (blue filled squares). The pink solid line refers to a power law of slope 0.75, which resembles the trend seen both in the simulations and the observations.

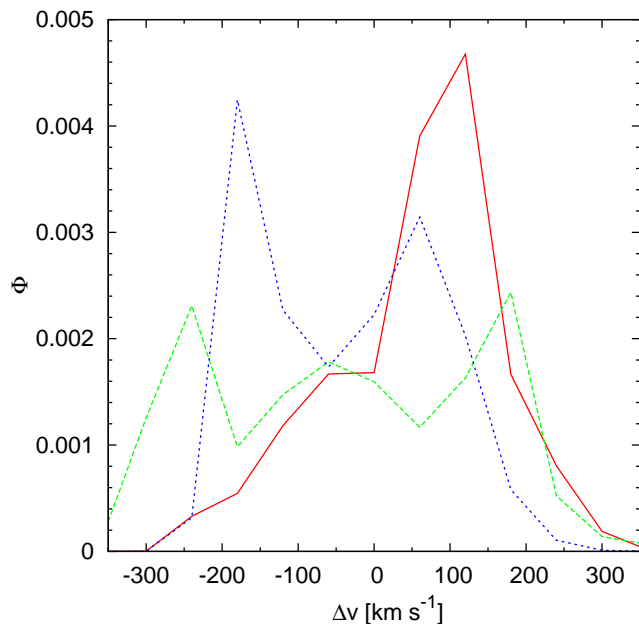


Figure 17. The kinematic components of three characteristic $L\alpha$ line profiles from CDB simulated galaxies, tentatively neglecting the effect of resonant scattering. These examples have between one to three dominant peaks, reflecting the relative orientations of the big cold streams and the line of sight.

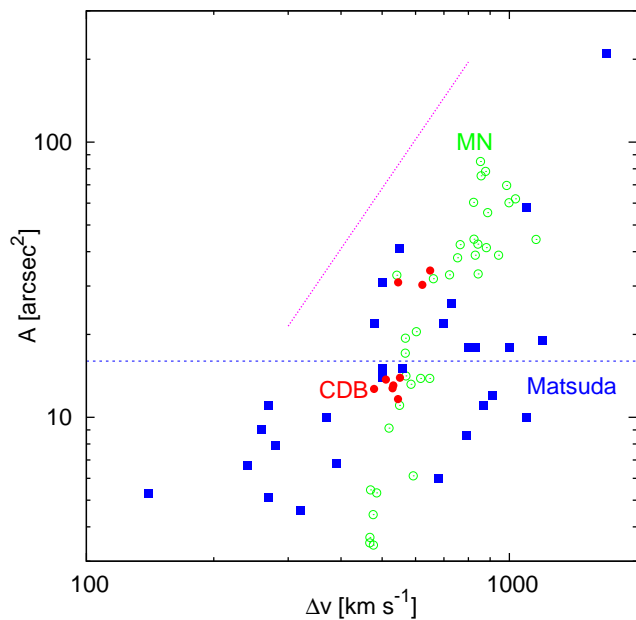


Figure 18. Isophotal area versus linewidth (FWHM) for LABs at $z = 3.1$. The simulated LABs from CDB (red filled circles) and MN (green open circles) are compared with $L\alpha$ emitters from Matsuda et al. (2006) (blue filled squares). The pink solid line refers to a power law of slope 2.25, which crudely resembles the general trend seen in the simulations and in the observations. The Δv deduced from the simulations is an underestimate and is subject to an artificially sharp lower bound at 436 km s^{-1} .

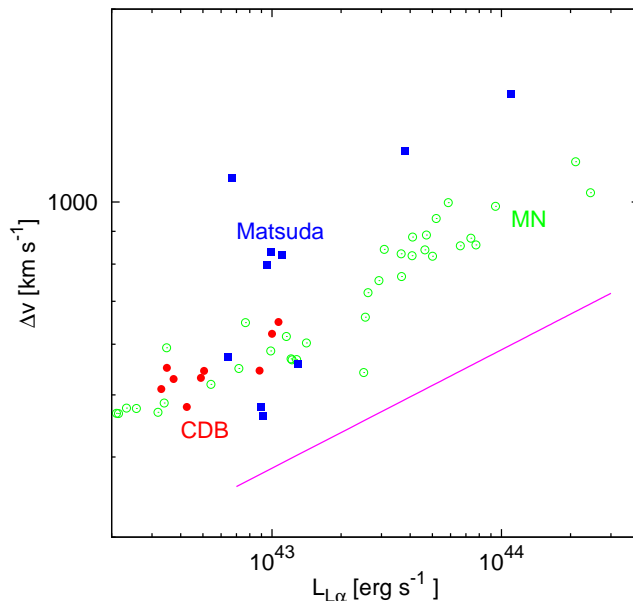


Figure 19. $L\alpha$ luminosity versus linewidth (FWHM) for LABs at $z = 3.1$. The simulated LABs from CDB (red filled circles) and MN (green open circles) are compared with LABs from Matsuda et al. (2004) and Matsuda et al. (2006) (blue filled squares). The pink solid line refers to a power law of slope 0.18, which crudely resembles the general trend seen in the simulations and in the observations, which are consistent within a factor of two.

heating, which was crudely approximated in §2, there is photoionisation by the UV background. Photoionisation effects by central sources such as stars and AGN were not simulated, and they are not expected to be substantial because of the shielding implied by the radial orientation of the cold streams. Before we address gravitational heating again, we should verify the contribution of the UV background.

A simple estimate is as follows. For an isotropic background with mean photon intensity $4\pi J^*$ and mean photon energy e , the rate at which energy is absorbed across a spherical surface of radius R is $\pi J^* e 4\pi R^2$. If we adopt for the metagalactic field at $z = 3$ a flux $\pi J^* \sim 5.5 \times 10^4 \text{ photons s}^{-1} \text{ cm}^{-2}$ and $e \sim 20 \text{ eV}$, we obtain a total UV heating rate into the virial radius $R_v \sim 100 \text{ kpc}$ of $2 \times 10^{42} \text{ erg s}^{-1}$. Even if all of the UV energy goes into heating the cold streams, the UV heating is small compared to the total $L\alpha$ luminosity of $\sim 10^{43} \text{ erg s}^{-1}$ and to the gravitational heating rate as estimated in §2. However, one should keep in mind that the MN simulation may overpredict the energy coming from the UV background when assuming that the gas is optically thin and the UV background is uniform.

To evaluate the relative contributions of gravitational heating and UV background in our actual simulation, we read from each grid cell of the simulation snapshot the instantaneous input rate of energy per unit volume by the UV flux, ϵ_{UV} , and subtract it from the $L\alpha$ emissivity computed in eq. (9), to obtain the relative contribution of gravitational heating in that cell,

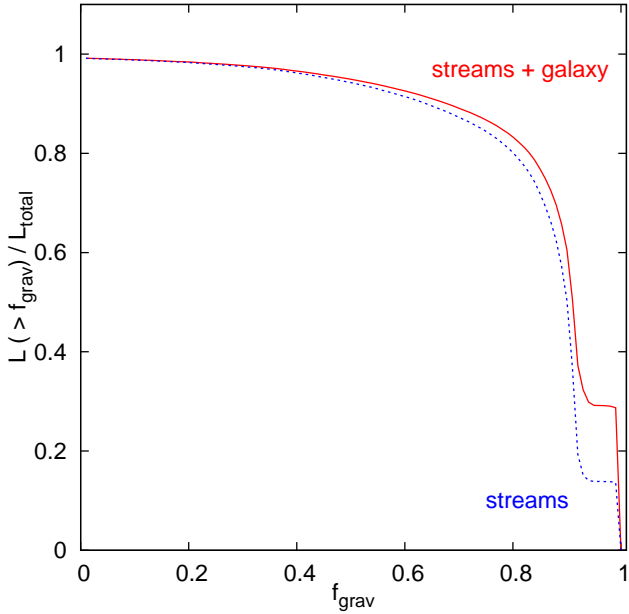


Figure 20. The role of gravitational heating versus photoionisation. Shown is the cumulative, luminosity-weighted distribution of the fraction of the energy that is provided by gravitational heating, f_{grav} , in the three CDB galaxies. The curves refer to the streams at $r = (0.2 - 1)R_v$ (dashed blue) and to the whole halo including the inner galaxy (solid red). The area under the curve implies that for the total CDB halo within R_v 86.8% of the energy input is gravitational, and only 13.2% is due to the UV background. The numbers are 84.2% and 15.8% respectively for the CDB halo between 0.2 and $1.0 R_v$.

$$f_{\text{grav}} \equiv \frac{\epsilon_{\text{L}\alpha} - \epsilon_{\text{UV}}}{\epsilon_{\text{L}\alpha}}. \quad (25)$$

Figure 20 shows the cumulative luminosity-weighted distribution of f_{grav} for the three CDB galaxies at $z = 2.3$. In this plot $f_{\text{grav}} = 0$ refers to cells where all the $\text{L}\alpha$ luminosity is driven by the UV background and $f_{\text{grav}} = 1$ corresponds to gravitational heating only. The area under the curve is the fraction of the total energy provided by gravity. In the CDB haloes this fraction is 86.8%, with only 13.2% due to the UV background for the total halo within R_v . It is 84.2% and 15.8% respectively for the halo between 0.2 and $1.0 R_v$. In more detail, if we focus, for example, on the cells of gas with the highest values of f_{grav} that contribute 0.8 of the total luminosity, we read from the figure that they all have $f_{\text{grav}} > 0.8$. This means that in the gas that is responsible for 80% of the $\text{L}\alpha$ luminosity, more than 80% of the energy is gravitational and less than 20% is due to the UV background. The fraction of the total energy provided by gravity in the MN haloes is 91.4%, with only 8.6% due to the UV background for the total halo within R_v . It is 79.5% and 20.5% respectively for the halo between 0.2 and $1.0 R_v$. We conclude that most of the $\text{L}\alpha$ emission from our simulated galaxies is indeed driven by gravitational heating.

The total luminosity as predicted by the simplified gravitational-heating toy model can be compared to the total $\text{L}\alpha$ luminosity that is actually produced in the simulations. We focus on the halo streams in the radius

range $r = (0.2 - 1.0)R_v$ in haloes of $M_v = 10^{12}M_\odot$ at $z = 3$. The toy-model estimate, based on eq. (7) and Fig. 1, is $E_{\text{heat}} \sim 10^{43} \text{ erg s}^{-1}$. A straightforward integral of the emissivity in the simulated galaxies over the same volume in the halo yields a comparable value (which can be read as L/f_α from Fig. 12). This implies that the toy-model parameter f_c should be of order unity, indicating that most of the gravitational energy is deposited in the cold streams.

We now return to Fig. 1, where we showed the gravitational heating toy-model prediction for the cumulative 3D luminosity profile. Shown in comparison is the corresponding $\text{L}\alpha$ luminosity profile as derived from the actual simulated CDB galaxies, averaged over the three galaxies. The similarity of the two profiles is remarkable. This implies, again, that the $\text{L}\alpha$ emission is indeed powered by gravitational heating, where the potential energy of the instreaming cold gas is radiated as $\text{L}\alpha$.

The cumulative luminosity profile can be fitted by a power law,

$$L(< r) \propto r^\alpha, \quad (26)$$

corresponding to a 3D luminosity density profile $\ell(r) \propto r^{\alpha-3}$. In the range $r = (0.1 - 0.4)R_v$, we find for the simulated luminosity $\alpha \simeq 0.8$, namely $\ell \propto r^{-2.2}$. This is consistent with the average surface-brightness profile $I(r) \sim r^{-1.2}$ measured in §9.1. The toy model predicts a similar power index over the same radius range. We also note that the density profile of cold gas follows a similar power law.

11 DISCUSSION AND CONCLUSION

Hydrodynamical cosmological simulations robustly demonstrate that massive galaxies at high redshifts were fed by cold gas streams, inflowing into dark-matter haloes at high rates along the cosmic web (Keres et al. 2005; Dekel & Birnboim 2006; Dekel et al. 2009). In this paper we have shown that these streams should be observable as luminous $\text{L}\alpha$ sources, with elongated irregular structures stretching for distances of over 100 kpc. The release of gravitational potential energy by the instreaming gas as it falls into the halo potential well is the origin of the $\text{L}\alpha$ luminosity, which ranges from 10^{42} to $10^{44} \text{ erg s}^{-1}$ for haloes in the mass range $10^{11} - 10^{13}M_\odot$ at $z \sim 3$. The predicted $\text{L}\alpha$ emission morphologies and luminosities make such streams likely candidates for the sources of observed high redshift $\text{L}\alpha$ blobs. Most of the gas in the cold streams is at temperatures in the range $(1 - 5) \times 10^4 \text{ K}$, for which the $\text{L}\alpha$ emissivity is maximised. The hydrogen gas densities in the streams are in the range $0.01 - 0.1 \text{ cm}^{-3}$, and are higher in clumps that flow with the streams, leading to the high surface brightnesses.

Using state-of-the-art cosmological AMR simulations with 70 pc resolution and cooling to below 10^4 K , and applying a straightforward analysis of $\text{L}\alpha$ emissivity due to electron impact excitation, we produced maps of $\text{L}\alpha$ emission from simulated massive galaxies at $z \sim 3$. We computed the average $\text{L}\alpha$ luminosity per given halo mass and the predicted luminosity function of these extended $\text{L}\alpha$ sources, with an uncertainty of ± 0.4 dex. The properties of the individual images resemble those of the observed LABs in terms of morphology and kinematics. The predicted luminosity function is close to the observed LAB luminosity

function. The simulated LABs qualitatively reproduce the observed correlations between the global LAB properties of $L\alpha$ luminosity, isophotal area and linewidth.

The LAB properties can be understood using a very simple toy model that accounts for gravitational heating of the inflowing gas. In comparison, the more elaborate toy model of DL09 predicts a steeper power-law relation between luminosity and halo mass (their Fig. 3, with $f_g = 0.2$). In the mass range $10^{12} - 10^{13} M_\odot$, DL09 predict luminosities in the range $1.5 \times 10^{42} - 2.5 \times 10^{44} \text{ erg s}^{-1}$. A comparison to our Fig. 12 indicates that they underestimate the luminosity at $M_v \sim 10^{12} M_\odot$ by a factor of a few. The DL09 toy model matches the observed luminosity function only after the predictions are boosted, trying to account for an overdense region of the universe. The association of the predicted LABs with massive haloes places them preferentially in overdense environments, as observed (Steidel et al. 2000; Matsuda et al. 2004, 2006), but this is already accounted for by the number density of haloes in a fair sample.

The association of observed LABs with star-forming LBGs (Hayashino et al. 2004), sub-millimetre galaxies (Chapman et al. 2001; Geach et al. 2005) or active galactic nuclei (Geach et al. 2009; Basu-Zych & Scharf 2004) is not surprising since star formation and AGN activity are triggered by the same process of streaming of cold gas into massive haloes. $L\alpha$ emission can be driven by any of these sources of energy. For example, in photoionised gas in star-forming regions the $L\alpha$ luminosity is $L_{L\alpha} = 1.5 \times 10^{42} \text{ SFR erg s}^{-1}$ where SFR is the star-formation rate (in $M_\odot \text{ yr}^{-1}$) for continuous star formation for a Kroupa initial mass function (Sternberg, Hoffmann & Pauldrach 2003). Thus the typical LAB luminosity of $10^{43} \text{ erg s}^{-1}$ would require $\text{SFR} \sim 10 M_\odot \text{ yr}^{-1}$. However, most of this radiation is likely absorbed by dust, and confined to the central galaxy.

A limitation of our AMR simulations arises from the artificial pressure floor imposed in order to properly resolve the Jeans mass. This may have an effect on the temperature and density of the cold gas in the streams, with potential implications on the computed $L\alpha$ emission. Still, the AMR code is the best available tool for recovering the stream properties. With 70 pc resolution and proper cooling below 10^4 K , the CDB simulations provide the most reliable description of the cold streams so far. The rather small correction that we had to apply to the luminosities extracted from the MN simulation indicates that the MN galaxies can be used to recover the mass and redshift dependence of the global stream properties and the scaling relations between them.

Another source of uncertainty has to do with the simplified way the ionisation by the UV background is handled in the simulations, and with the post-processing calculation of the ionisation state of the cold gas. In the CDB simulations, the centres of the streams, where the gas density is higher than 0.1 cm^{-3} , were assumed to be self-shielded against the UV background, in agreement with our analytic estimates in §4. The ionisation state of the gas, which is a key ingredient in evaluating the $L\alpha$ emissivity, was computed in post-processing assuming CIE. Cooling rates were computed for the given gas density, temperature, metallicity, and UV background based on CLOUDY (CDB) or assuming ionisation equilibrium for H and He, including both collisional- and photo-ionisation

(MN). Photoionisation is neglected since the streams are sufficiently thick to be self-shielded. An alternative calculation using CLOUDY yielded lower fractions of neutral hydrogen at $n \leq 0.01 \text{ cm}^{-3}$, and total luminosities that are typically three times smaller than obtained using CIE. This calculation assumed that each cell, with a given hydrogen density n , is in the middle of a uniform slab of thickness 1 kpc. Based on our estimates of self-shielding, eq. (17), we adopt the CIE results as the more reliable approximation.

In our computations so far we did not consider the radiative transfer of $L\alpha$ photons through the streams, or through the intervening intergalactic medium. We assume that most of the radiation emitted at $z \sim 3$ will reach the observer at $z = 0$ without undergoing significant attenuation. Resonant line scattering in the optically thick streams will tend to spread out the $L\alpha$ emission region, while the repeated Doppler shifts broaden the line profiles, and the increased path length of the random walk amplifies the absorption by dust. Such effects are expected to modify the images and line profiles, but to have only a small effect on the total $L\alpha$ luminosity. An analysis of $L\alpha$ emission from our simulated galaxies including the effects of radiative transfer and dust absorption and a more accurate treatment of photoionisation from stars will be presented in a forthcoming paper (Kasen et al, in preparation).

Other hydrogen emission lines, such as $L\beta$ or $H\alpha$, are expected to be two orders of magnitude less luminous than $L\alpha$ in our model (Baldwin 1977; Miller 1974). The column densities of $N_{\text{HI}} \sim 10^{20} \text{ cm}^{-2}$ in the cold streams should also be detectable as $L\alpha$ absorption in quasar spectra (Prochaska 1999; Wolfe, Gawiser & Prochaska 2005). Considering all the galaxies that are intersected by a line of sight to a background quasar with an impact parameter $< R_v$, we crudely estimate from the simulations that absorption by $N_{20} > 1$ hydrogen should be detected in $\sim 20\%$ of the galaxies. Alternatively, $L\alpha$ photons that are emitted from the central galaxy should be absorbed in the radial streams feeding the same galaxy at $N_{20} > 10$, but only in $\sim 5\%$ of the galaxies. The streams could also be detectable as low-ionisation metal absorbers (e.g. Gnat & Sternberg 2007) as long as the metallicity in the streams is greater than ~ 0.01 solar (paper in preparation).

Our results support the idea that the observed LABs are direct detections of the cold streams that drive the evolution of massive galaxies at high redshifts. Even though the observed LABs are sometimes associated with central sources that are energetic enough to power the observed $L\alpha$ emission, such as starbursts and AGNs, these central sources are very different from each other in the different galaxies, and in many LABs they are absent altogether (Yang et al. 2008; Geach et al. 2007). The gravitational heating associated with the inflowing cold streams is a natural mechanism for driving the extended $L\alpha$ cooling radiation observed as LABs, and this extended $L\alpha$ emission is inevitable in most high-redshift galaxies.

ACKNOWLEDGEMENTS

The computer simulations were performed at NERSC, LBNL, and at the Barcelona Centro Nacional de Supercomputaci3n as part of the Horizon collaboration.

We thank Yuchi Matsuda, Kim Nilson and Masami Ouchi for sharing observational data with us. We acknowledge stimulating discussions with Nicolas Bouché, Michele Fumagalli, Orly Gnat, Daniel Kasen, Anatoly Klypin, Kamson Lai, Piero Madau, Ari Maller, Mark Mozena, Eyal Neistein, Hagai Netzer, and Jason X. Prochaska. This research has been partly supported by an ISF grant, by GIF I-895-207.7/2005, by a France-Israel Teamwork in Sciences, by the Einstein Center at HU, by NASA ATP NAG5-8218 at UCSC. We thank the DFG for support via German-Israeli Project Cooperation grant STE1869/1-1.GE625/15-1. Tobias Goerdt is a Minerva fellow and Daniel Ceverino is a Golda Meir fellow.

REFERENCES

- Adams T. F, 1972, *ApJ*, 174, 439
Adams T. F, 1975, *ApJ*, 201, 439
Baldwin J. A, 1977, *MNRAS*, 178, 67
Basu-Zych A, Scharf C, 2004, *ApJ*, 615, 85
Birnboim Y, Dekel A, Neistein E, 2007, *MNRAS*, 380, 339
Birnboim Y, Dekel A, 2003, *MNRAS*, 345, 349
Bullock J. et al, 2001, *MNRAS*, 321, 559
Callaway J, Unnikrishnan K, Oza D. H, 1987, *PhRvA*, 36, 2576
Ceverino-Rodriguez D, 2008, Ph.D. Thesis
Ceverino D, Dekel A, Bournaud F, 2009, arXiv:0907.3271 [astro-ph.CO]
Ceverino D, Klypin A. A, 2009, *ApJ*, 695, 292
Chapman S. C, Lewis G. F, Scott D, Richards E, Borys C, Steidel C. C, Adelberger K. L, Shapley A. E, *ApJ*, 548, 17
Dalla Vecchia C, Schaye J, 2008, *MNRAS*, 387, 1431
Dekel A, Birnboim Y, 2006, *MNRAS*, 368, 2
Dekel A, Birnboim Y, 2008, *MNRAS*, 383, 119
Dekel A, Birnboim Y, Engel G. et al, 2009, *Nature*, 457, 451
Dekel A, Sari R, Ceverino D, 2009, 2009, *ApJ*, 703, 785
Dijkstra M, Loeb A, 2009, *MNRAS*, 400, 1109, DL09
Draine B, Lee H. M, 1984, *ApJ*, 285, 89
Draine B, 2003, *ARA&A*, 41, 241
Dubois Y, Teyssier R, 2008, *A&A*, 477, 79
Elmegreen D. M, Elmegreen B. G, Ferguson T, Mullan B, 2007, *ApJ*, 663, 734
Fardal M. A, Katz N. G, Jeffrey P, Hernquist L, Weinberg D. H, Davé R, 2001, *ApJ*, 562, 605
Faucher-Giguere C, Prochaska J. X, Lidz A, Hernquist L, Zaldarriaga A, 2008b, *ApJ*, 681, 831
Ferland G. J, Korista K. T, Verner D. A, Ferguson J. W, Kingdon J. B, Verner E. M, 1998, *PASP*, 110, 761
Förster Schreiber N. M. et al, 2006, *ApJ*, 645, 1062
Förster Schreiber N. M. et al, 2009, *ApJ*, 706, 1364
Furlanetto S. R, Schaye J, Springel V, Hernquist L, 2005, *ApJ*, 622, 7
Furlanetto S. R, Schaye J, Springel V, Hernquist L, 2003, *ApJ*, 599, 1
Geach J. E. et al, 2005, *MNRAS*, 363, 1398
Geach J. E, Smail I, Chapman S. C, Alexander D. M, Blain A. W, Stott J. P, Ivison R, 2007, *ApJ*, 655, 9
Geach J. E. et al, 2009, *ApJ*, 700, 1
Genel S. et al, 2008, *ApJ*, 688, 789
Genzel R. et al, 2006, *Nature*, 442, 786
Genzel R. et al, 2008, *ApJ*, 687, 59
Gnat O, Sternberg A, 2007, *ApJS*, 168, 213
Grevesse N, Sauval A. J, 1998, *SSRv*, 85, 161
Haardt F, Madau P, 1996, *ApJ*, 461, 20
Haiman Z, Spaans M, Quateart E, 2000, *ApJ*, 537, 5
Haiman Z, Rees M. J, 2001, *ApJ*, 556, 87
Harrington J. P, 1973, *MNRAS*, 162, 43
Hayashino T. et al, 2004, *AJ*, 128, 2073
Hui L, Gnedin N. Y, 1997, *MNRAS*, 292, 27
Jimenez R, Haiman Z, 2006, *Nature*, 440, 501
Johansson P. H, Naab T, Ostriker J. P, 2009, *ApJ*, 697, 38
Katz N, Hernquist L, Weinberg D. H, 1992, *ApJ*, 399, 109
Kennicutt R. C, 1998, *ApJ*, 498, 541
Keres D, Katz N, Weinberg D. H, Davé R, 2005, *MNRAS*, 363, 2
Keres D, Katz N, Fardal M, Davé R, Weinberg D. 2009, *MNRAS*, 395, 160
Khochfar S, Ostriker J. P, 2008, *ApJ*, 680, 54
Komatsu E. et al, 2009, *ApJS*, 180, 330
Kravtsov A. V, 2003, *ApJ*, 590, 1
Kravtsov A. V, Klypin A. A, Khokhlov A. M, 1997, *ApJS*, 111, 73
Matsuda Y. et al, 2004, *AJ*, 128, 569
Matsuda Y, Yamada T, Hayashino T, Yamauchi R, Nakamura Y, 2006, *ApJ*, 640, 123
Miller G. E, Scalo J. M, 1979, *ApJS*, 41, 513
Miller J. S, 1974, *ARA&A*, 12, 331
Mori M, Umemura M, Ferrara A, 2004, *ApJ*, 613, 97
Navarro J. F, Frenk C. S, White S. D. M, 1997, *ApJ*, 490, 493
Neistein E, van den Bosch F, Dekel A, 2006, *MNRAS*, 372, 933
Neistein E, Dekel A, 2008, *MNRAS*, 383, 615
Neufeld D. A, 1990, *ApJ*, 350, 216
Nilsson K. K, Fynbo J. P. U, Møller P, Sommer-Larsen J, Ledoux C, 2006, *A&A*, 452, 23
Ocvirk P, Pichon C, Teyssier R, 2008, *MNRAS*, 390, 1326
Ouchi M, Ono Y, Egami E. et al, 2009, *ApJ*, 696, 1164
Prochaska J. X, 1999, *ApJL*, 511, L71
Rees M. J, 1989, *MNRAS*, 239, 1
Robertson B. E, Kravtsov A. V, 2008, *ApJ*, 680, 1083
Saito T, Shimasaku K, Okamura S, Ouchi M, Akiyama M, Yoshida M, 2006, *ApJ*, 648, 54
Scarlata C. et al, 2009, *ApJ*, 706, 1241
Schaye J, Dalla Vecchia C, 2008, *MNRAS*, 383, 1210
Scharf C, Smail I, Ivison R, Bower R, van Breugel W, Roland M, 2003, *ApJ*, 596, 105
Sheth R. K, Tormen G, 1999, *MNRAS*, 308, 119
Smith D. J. B, Jarvis M, 2007, *MNRAS*, 378, 49
Springel V, Hernquist L, 2003, *MNRAS*, 339, 289
Stark D. P, Swinbank A. M, Ellis R. S, Dye S, Smail I. R, Richard J, 2008, *Nature*, 455, 775
Steidel C. C, Adelberger K. L, Dickinson M, Giavalisco M, Pettini M, Kellogg M, 2000, *ApJ*, 532, 170
Steidel C. C, Adelberger K. L, Shapley A. E, Pettini M, Dickinson M, Giavalisco M, 2000, *ApJ*, 532, 170
Sternberg A, Hoffmann T. L, Pauldrach A. W. A, 2003, *ApJ*, 599, 1333
Teyssier R, 2002, *A&A*, 385, 337
Truelove J. K, Klein R. I, McKee C. F, Holliman J. H, Howell L. H, Greenough J. A, 1997, *ApJ*, 489, 179

- Wolfe A. M, Gawiser E, Prochaska J. X, 2005 ARA&A, 43, 861
Woosley S. E, Weaver T. A, 1995, ApJS, 101, 181
Yang Y, Zabludoff A, Tremonti C, Eisenstein D, Davé R, 2009, ApJ, 693, 1579
Yepes G, Kates R, Khokhlov A, Klypin A, 1997, MNRAS, 284, 235